A Tunable MEMS-Enabled Frequency Selective Surface

by

Mojtaba Safari

A Thesis submitted to the Faculty of Graduate Studies of

The University of Manitoba

in partial fulfilment of the requirements of the degree of

MASTER OF SCIENCE

Department of Electrical and Computer Engineering

University of Manitoba

Winnipeg

Abstract

A frequency selective surface (FSS) based on switchable slots in the ground plane is presented. The switching is done using an actuating MEMS bridge over the slot. The intent is to demonstrate the control of the resonance frequency of the FSS by deflecting the bridge. It is shown that by applying a voltage between the bridge and the ground plane, the bridge displaces and changes the system capacitance which in turn changes the resonance frequency. Two analyses are presented; (1) Electromechanical analysis to show how the bridge deflects by the voltage, (2) Electromagnetic analysis to show how the resonance frequency changes by the bridge deflection. The device was fabricated and tested. The measurement results are presented for two up and down positions of the MEMS bridge to verify the correctness of the theory and design.

Acknowledgment

Dedicated to all the political prisoners and prisoners of conscience in Iran

Table of Contents

List of Tables

List of Figures

viii

Chapter 1

Introduction

1.1.   Background of the Problem

A frequency selective surface (FSS) is similar to a band-pass filter but for electromagnetic waves. An ideal FSS only passes or reflects one specific frequency. Since the introduction of Frequency Selective Surfaces, researchers have examined different methods to make a reconfigurable FSS by changing either, or both, the electrical properties or physical geometry of the FSS. Explored concepts included the use of ferrite materials, PIN diodes, varactors, liquids, optimal illuminated semiconductors, and MEMS. MEMS-based frequency selective surfaces are amongst the newest methods, however, presented concepts so far have some disadvantages such as complexity and cost. The two following examples demonstrate these drawbacks and the need to achieve a more simple design:

1. Schoenlinner et al. demonstrated a four-legged loaded element with tunable capacitive loading bridges to provide a switchable surface in Ka-band frequency [1]. Looking at the design in Figure 1, one notices the complexity of the structure.

2. Zendejas et al. used an electromagnetic field to tilt ferromagnetic dipoles [2] (Figure 2). This technique has the disadvantage of requiring an external magnetic source.

A review of existing FSS designs will be discussed in Chapter 2.
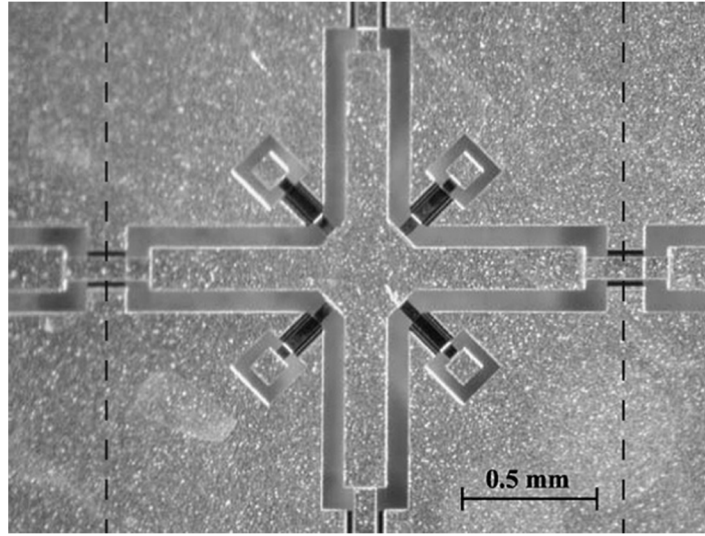
Figure 1: Four-legged element with capacitive loading bridges [1] (Copyright IEEE).
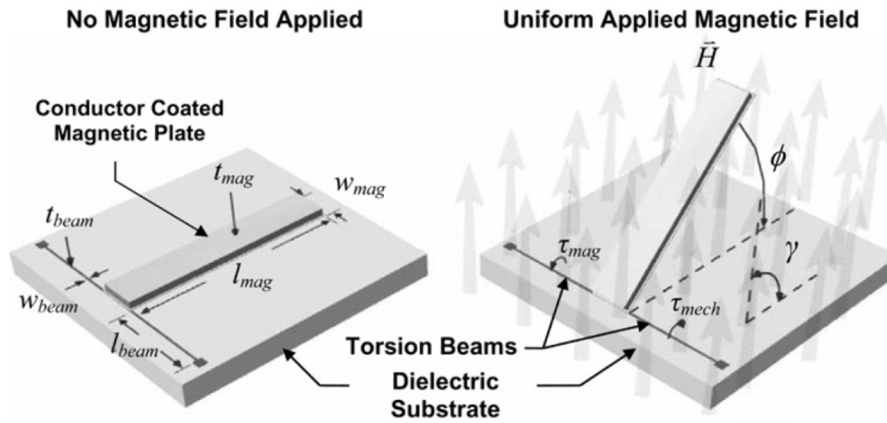
Figure 2: Tilting ferromagnetic dipoles [2] (Copyright IEEE).

1.2.   Statement of the Problem

The research on the subject of tunable FSS is extensive and using a MEMS switch to tune an FSS is not new, however, the existing MEMS designs are complex. Current MEMS switch enabled designs use the MEMS switch to connect to secondary elements, which complicates the design. For example, the design of Figure 1 used multiple MEMS

switches to connect capacitive elements to the FSS. My thesis undertakes the design of the FSS together with a MEMS bridge to avoid a complicated design. The focus of my thesis is a MEMS enabled FSS by using an array of slots in the ground plane. Each slot is loaded by a MEMS bridge which can be deflected by an actuation voltage, thereby changing the loading and so the frequency of the FSS. The structure is illustrated in Figure 3. The structure benefits from a straightforward and easy-to-fabricate design with the capability of increasing the number of bridges to obtain more frequency shift. The final purpose is to show that the resonance frequency of the FSS can be changed by deflecting the MEMS bridge.
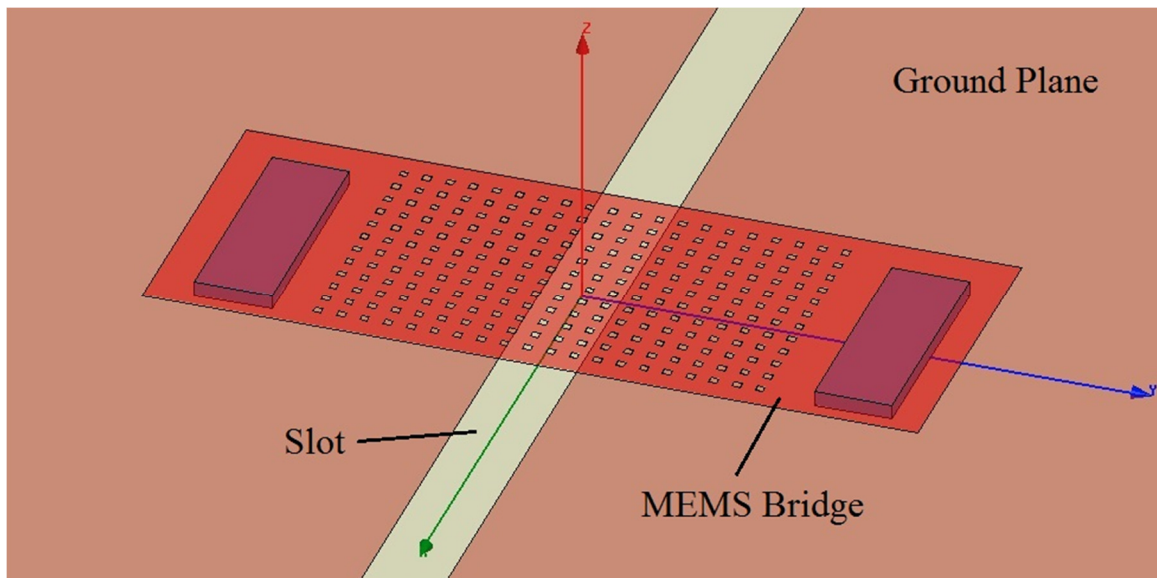
Figure 3: Slot loaded by a MEMS bridge.

1.3.   Purpose of the Study

Three major efforts have been undertaken to build the FSS of this thesis; simulation, fabrication and measurement. The design and its considerations will be discussed and compared with the simulations. The goal is to show that the simulation results agree with

3

the measurement ones. For the simulation part, COMSOL Multiphysics was used for the mechanical analysis and HFSS for the electromagnetic analysis. These simulations have been widely used for such problems by other groups and they have proven their reliability for research purposes. For the fabrication, the facilities of the Nano-Systems Fabrication Laboratory (NSFL), in the Electrical and Computer Engineering Department, University of Manitoba, were used. The RF measurements were done in the Applied Electromagnetics Laboratory.

The simulation and measurement results were undertaken in the range of X-band, and a waveguide was used to test the FSS. These results show that the resonance frequency can be changed by the integrated MEMS bridge.

1.4.   Summary of Thesis

The literature review is discussed in Chapter 2. The review covers both MEMS and FSS subjects. In Chapter 3, design and simulation are discussed where it is shown in detail how to use the software to simulate the structures. Chapter 4 discusses the fabrication process and elaborates the recipes, methods and equipments which were used. The fabrication problems and their solutions and reasons are also discussed. After fabrication, testing of the fabricated devices is shown in Chapter 5. The measurement data including the tables, plots, etc., are shown. The comparison between simulation and measurement results is made and further discussion explains the problems and solutions. At the end of the chapter, a new design is introduced to improve the old design. The simulation results for the new design prove the correctness of the solutions. Chapter 6

presents the conclusions, a summary of what has been achieved in the thesis, and future works.

In this thesis, a new tunable FSS is introduced and an electrostatic MEMS switch is developed that features eliminating the need for pull-down electrode and also the bias bridges. These make the fabrication process easier. In the fabrication part of this thesis, a new lithography process was developed and optimized for small holes. In the EM part of this thesis, criteria for the conductivity of the sacrificial layer in the MEMS structures used in frequency selective surfaces are introduced.

Chapter 2

Review of the Literature

This chapter will describe the background in three topic areas relevant to this thesis. First, an introduction to MEMS will be given. Second, RF-MEMS switches will be discussed. Since this thesis uses a MEMS switch integrated into the FSS to change its frequency response, it is important to describe both MEMS and FSS topics. Third, current research in frequency selective surfaces will be described.

2.1. Micro-Electro-Mechanical Systems

Micro-Electro-Mechanical Systems (MEMS) refers to a technology in which both mechanical devices and electronic devices are miniaturized and operate together. Usually the electronics is used to drive the mechanical part. Such technology can benefit from low energy loss, small size, high sensitivity, good thermal/electrical isolation, and high strength to mass ratio. MEMS technology has been widely used to fabricate different devices such as sensors/actuators, switches, resonators, fuel cells, phase shifters and motors/gears.

MEMS fabrication involves different techniques that are already commonly used in semiconductor technology. There lies profound literature about MEMS, but to avoid an

extensive review, the following sections describe only the major techniques which have been used for this thesis.

2.1.1. Sputtering

Sputtering is a method of deposition in which an RF or DC voltage is applied between a substrate and a target made of the desired material for deposition. The electric field ionizes the gas (typically argon) inside the vacuum chamber and accelerates the ions toward the target. The bombarding of the target removes atoms from the target some of which then settle on the substrate.

DC plasma is used for good conductors such as metals. For non-/semi- conductors, RF plasma is used to prevent charge accumulation on the target which will eventually stop the ion bombardment. In an RF plasma, the changing polarity allows the accumulated charges to be depleted. Figure 4 shows the MRC 8667 sputtering system in the NSFL, which was used for this thesis. Further information about sputtering can be found in [3–6].

Figure 4: NSFL MRC 8667 sputtering system.

2.1.2. Lithography

Lithography is perhaps one of the most important parts of the microfabrication technology. Lithography is used to transfer a design from a mask onto a substrate. Lithography consists of spinning photoresist, baking it dry, exposing it to UV light, and developing it.

Photoresist is a liquid polymer which becomes soluble (positive photoresist) or insoluble (negative photoresist) after exposure to UV light. The photoresist is spread over the sample using a spinner. The spinner holds onto the substrate using vacuum suction

while it spins it to let the photoresist spread over the sample. Before exposure, the photoresist should be baked to harden it. Figure 5 shows the oven in the NSFL, which was used for this thesis.

Figure 5: NSFL Oven

After baking, the photoresist has to be exposed to UV light through a photomask to transfer a pattern onto it. A photomask is a piece of glass which has a chrome pattern on it. A mask aligner is used to align the substrate with respect to the photomask so that the pattern is transferred in the position needed with a good accuracy. Figure 6 shows the ABM mask aligner in the NSFL, which was used for this thesis.
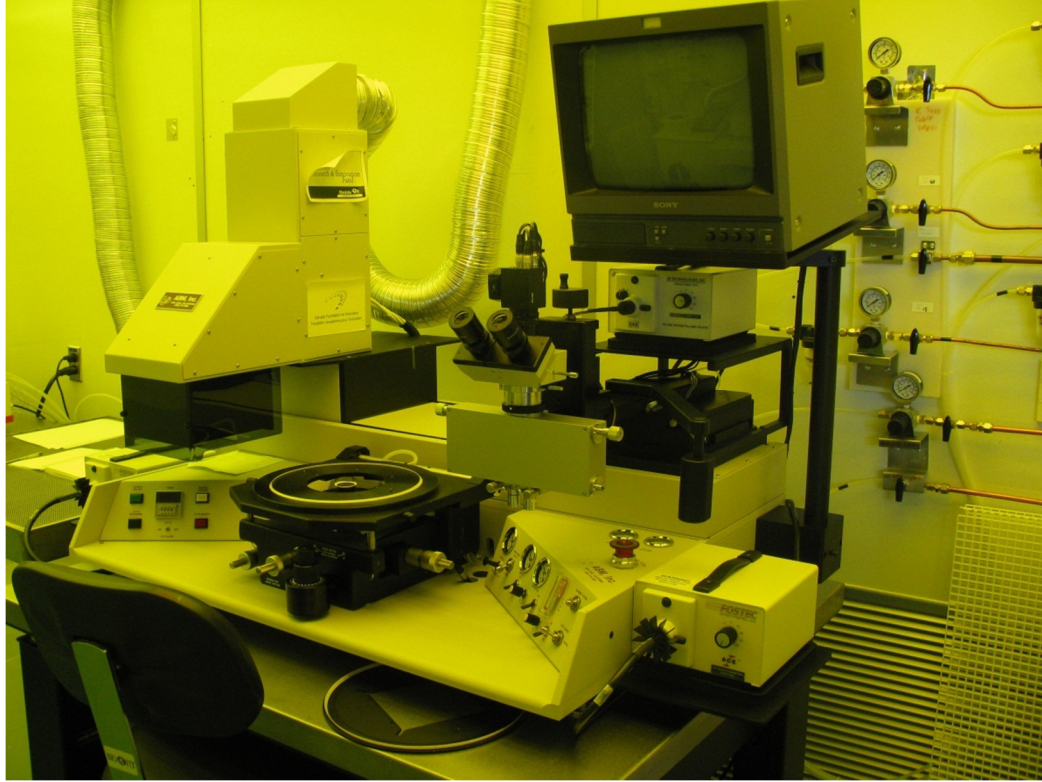
Figure 6: NSFL ABM mask aligner.

Developing is done after the exposure. This process etches the photoresist that was exposed to UV light (positive photoresist). The developer is a liquid solution which etches only the exposed or unexposed areas depending on the type of the photoresist. Figure 7 shows the spinner/developer unit in the NSFL, which was used for this thesis.
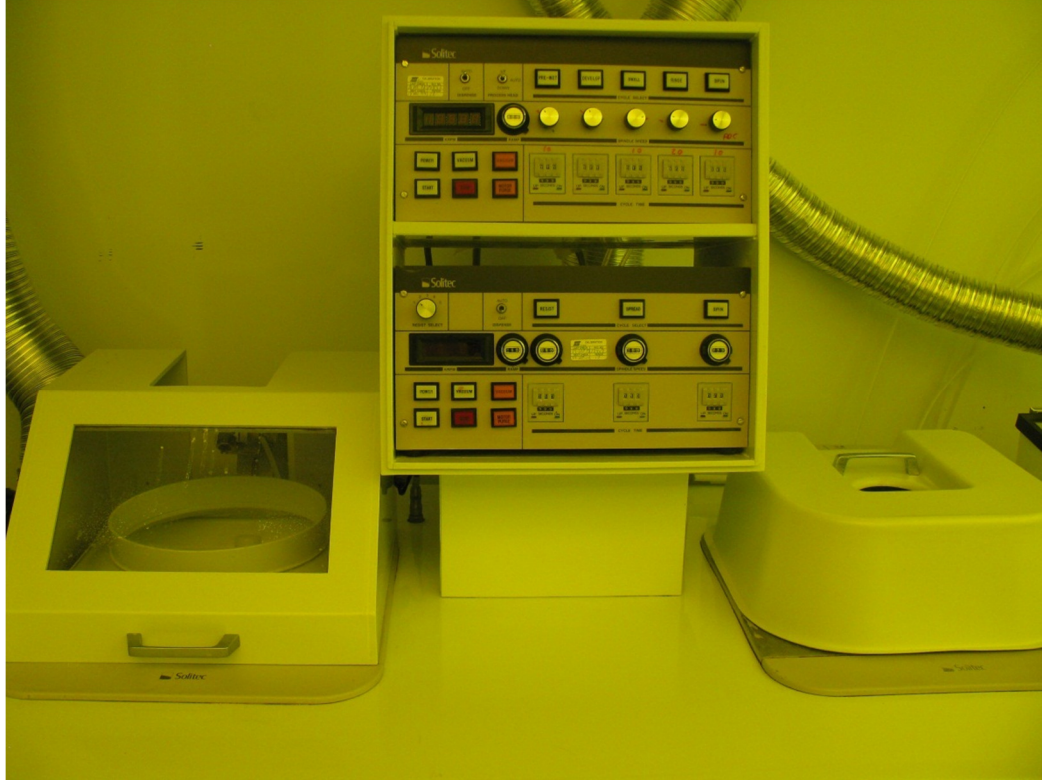
Figure 7: NSFL spinner/developer unit.

Exposure and developing times are two influential parameters in lithography. To transfer the mask pattern onto the photoresist, one has to have the right exposure and developing times. Any other timing (less or more than necessary) will scale the pattern. The correct exposure and developing times depend on the different parameters such as the type of the photoresist, humidity, UV light intensity, and thickness of the photoresist, which in turn is determined by the spinning speed. Further information about lithography can be found in [3–6].

2.1.3. Etching

Etching is the process of removing some parts of a material. The areas that are not to be etched have to be covered by either photoresist (in a lithography process) or another protection layer.

One can separate etching into two different types; isotropic and anisotropic. In isotropic etching, the vertical and horizontal etch rates are ideally similar. In other words, the etchant etches the material in all directions with the same speed. If you think of a circular opening in the surface of a material exposed to an isotropic etchant, the result will be ideally a semi-sphere under the opening (Figure 8). Whereas an anisotropic etchant will result ideally in a trench with vertical sidewalls (Figure 9).
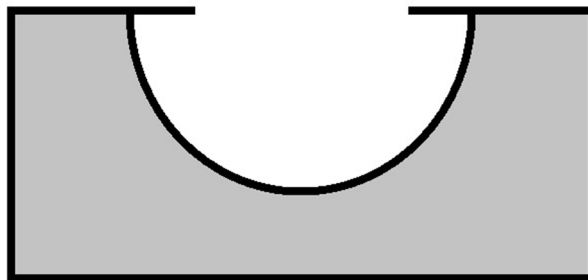
Figure 8: Isotropic etching
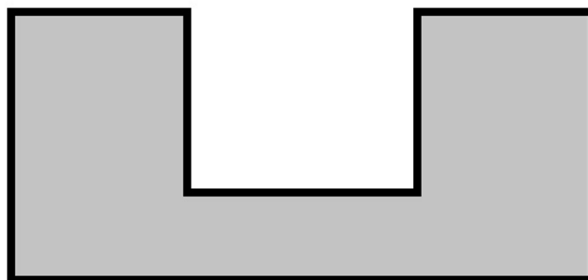
Figure 9: Anisotropic etching

2.1.3.1. Wet etching

In wet etching, a liquid is used as the etchant. Wet etching is usually isotropic, however, the etch rates can be different for different crystal orientations, which makes the etching anisotropic. The etch rate also varies with temperature; therefore to accelerate the etching process, one can heat up the solution. In the NSFL, wet etching is done at a wet deck such as those shown in Figure 10. Further information about wet etching can be found in [3–6].

Figure 10: NSFL wet decks.

2.1.3.2. Dry etching

In dry etching, either a gas or plasma is used as the etchant. In the case of using non-ionized gas, the etching is a chemical process. While for ionized plasma gas, the process

can be either chemical, or physical (with ions bombarding the surface), or sometimes a combination of both.

Unlike wet etching and gas etching, plasma etching is more flexible and has many parameters to play with. Plasma etching systems can be categorized in two major setups; capacitively coupled plasma (CCP), and inductively coupled plasma (ICP). In CCP setup, an RF voltage is applied to two electrodes and creates plasma which in turn bombards the substrate and etches it. In ICP setup, a similar procedure occurs but using a coil instead of two electrodes. There are some plasma etching systems that have both setups with two different power supplies; one power supply is used to feed the coil (called ICP power supply), and the other power supply is used to feed the two electrodes (called RIE power supply). ICP augments and determines the amount of ions in the chamber, whereas RIE generates ions and determines the power with which the ions hit the substrate. Therefore, increasing RIE power can provide a more physical etching which is normally anisotropic as opposed to chemical etching that is isotropic. Another effective parameter is pressure. At higher pressures, ions have a greater probability of hitting other gas molecules, randomizing their motion, which makes the etching more isotropic. Figure 11 and Figure 12 show the plasma etching system and the XeF_2 etching systems in the NSFL, respectively. Further information about dry etching can be found in [3–6].

Figure 11: NSFL plasma etching system.

Figure 12: NSFL XeF_2 etching system.

2.2.   RF-MEMS Switches

RF-MEMS switches are micro-switches that are used to switch RF frequencies. In regular semiconductor switches, losses at high GHz frequencies can be high. This is the major motivation for using MEMS switches. There are different applications of RF-MEMS switches such as phased arrays, reconfigurable apertures, switching networks, and phase shifters.

Depending on the method used to provide actuation for the switch, there are different classifications of RF MEMS switches; e.g. electrostatic, magnetic, thermal, and piezoelectric. The electrostatic method is used more often than the others because of the

ease of fabrication and low power operation; therefore this introduction concentrates more on electrostatic MEMS switches.

There are some advantages in using MEMS switches over PIN diode and FET (semiconductor switches); however it should be mentioned that these advantages occur mostly with electrostatic MEMS switches [7]:

- Electrostatic actuated MEMS switches possess near zero power consumption in steady state. No current flows between the electrodes in the open or closed position leading to a very small power dissipated.

- High isolation due to air gap between the electrodes.

- Low insertion loss.

- Very linear response to strain (material deformation).

- Low cost RF MEMS switches can be fabricated using surface micromachining techniques.

Some disadvantages compared to semiconductor switches are:

- Low speed (typically only millisecond and microsecond speeds).

- Low signal power handling.

- High voltage drive.

- Low reliability. Typically a reliability of 20-200 billion cycles is needed in some applications but RF MEMS switches typically only reach up to 0.1-10 billion cycles.

- Packaging. Because of the fragility of the MEMS structures, they need to be packaged in inert atmosphere and low humidity, which is expensive.

2.2.1. Electrostatic Actuation

Most of the electrostatic MEMS switches are based on attraction force between two electrodes. Hence we begin with the study of electromechanical equations applied to such structures.

For a massless rectangular bridge anchored at its two ends actuated by a distributed force, the deflection is given by [3]:

$$y(x) = \frac{\rho x^2}{24EI}(L - x)^2 \tag{1}$$

where L is the length of the bridge, E is Young's Modulus, ρ is the force per unit length, and I is the momentum of inertia. ρ is given by:

$$\rho = \frac{F}{L} \tag{2}$$

where F is the force. I is given by:

$$I = \frac{wt^3}{12} \tag{3}$$

where w is the width and t is the thickness of the bridge. F which is the electrostatic force between two plates can be calculated from:

$$F = \frac{\epsilon A V^2}{2d^2} \qquad (4)$$

where A is the area of overlap of the plates, V is the applied voltage and d is the distance between the two plates. Also the resonant frequency of a bridge is given by [3]:

$$\omega_n = 22.5 \sqrt{\frac{EI}{mL^3}} \qquad (5)$$

where m is the mass of the bridge.

There are two major types of electrostatic MEMS switches, shunt and series. In shunt switches, one port is connected to the ground, whereas in series switches, no port is connected to the ground.

2.2.1.1. Shunt Switches

This type of switch can be built on either microstrip lines (Figure 13) or coplanar waveguide lines (Figure 14). A simple fabricated shunt switch is shown in Figure 15.
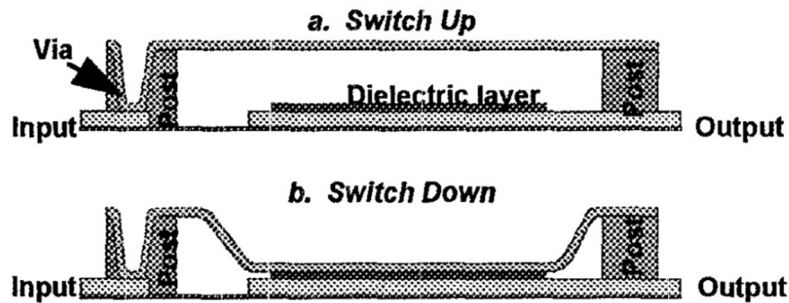
Figure 13: Shunt switch built on microstrip line [8] (Copyright IEEE).
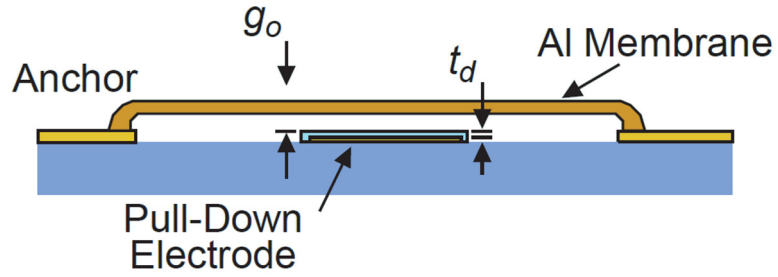
Figure 14: Shunt switch built on coplanar waveguide line [7] (Copyright IEEE).
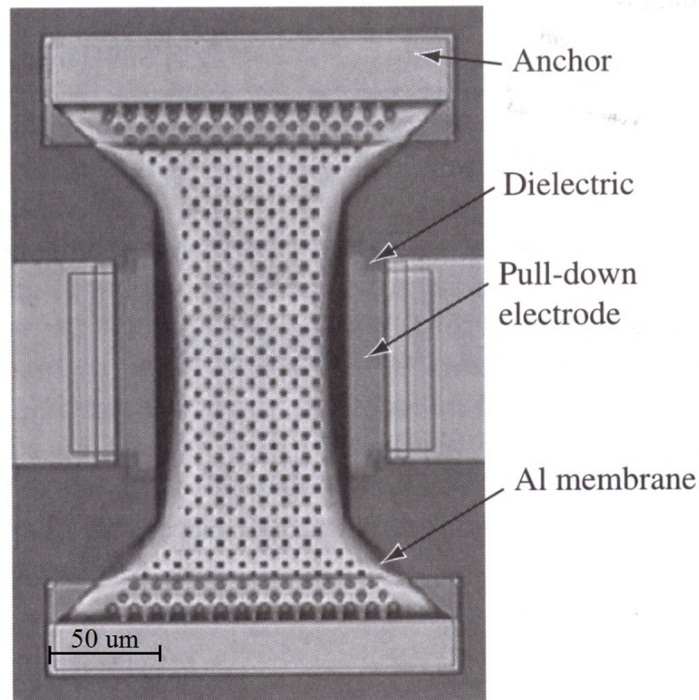
Figure 15: A fabricated shunt switch [9] (Copyright IEEE).

2.2.1.2. Series Switches

Series switches are divided in two types, broadside and inline. In the broadside design, the switch consists of a non-conducting supporting beam with a conducting tip that connects two ports in the closed position. Whereas in the inline design, the beam itself is a conductor which connects two ports together. An advantage of the inline design compared to the broadside is that the inline is more compact. On the other hand, in the broadside design two pull-down electrodes can be used which lowers the actuation

20

voltage. Figure 16 shows the two types of series switches. Two simple fabricated inline and broadside switches are shown in Figure 17 and Figure 18, respectively.
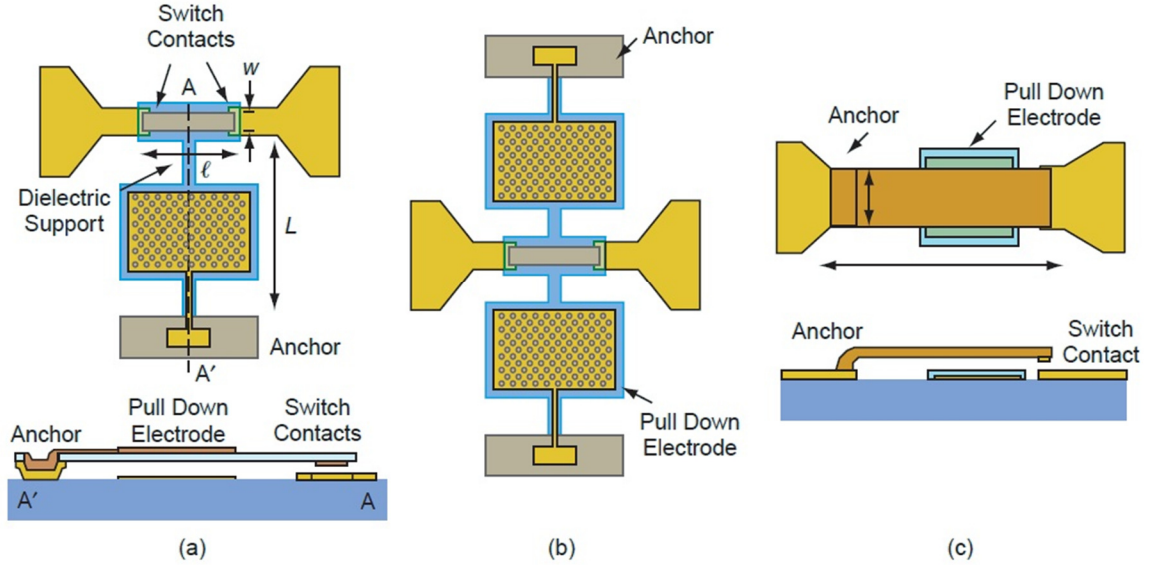
Figure 16: Two types of series switches (a) Broadside with one pull-down electrode, (b) Broadside with two pull-down electrodes and (c) Inline [7] (Copyright IEEE).
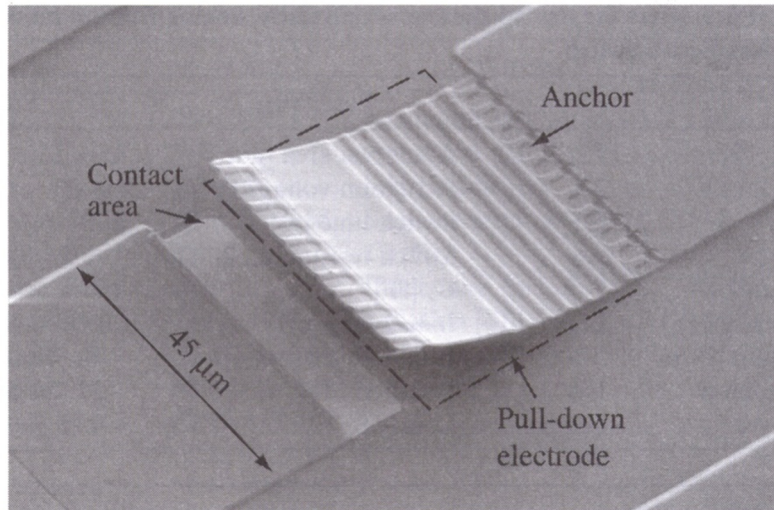
Figure 17: Stressed inline series switch [9] (Copyright IEEE).
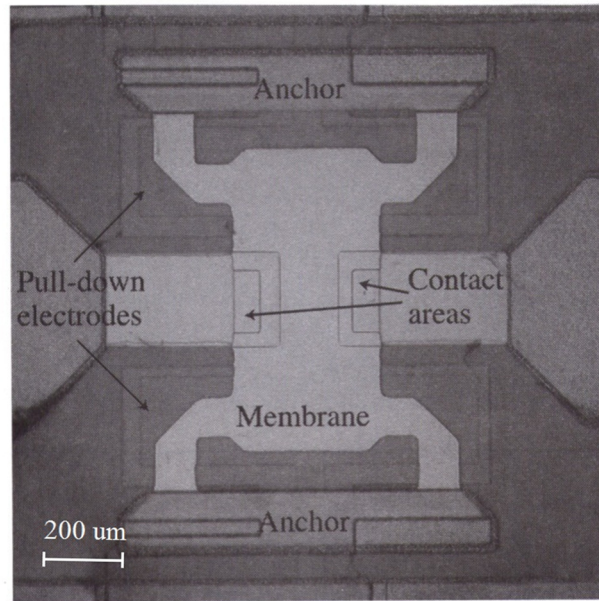
Figure 18: Broadside series switch [9] (Copyright IEEE).

2.2.2. Lateral Force Switches

Two lateral force switch configurations are shown in Figure 19. The main benefit of this type of switch is that all the components such as the actuator, contacts, conductor paths and support structure can be fabricated in one lithography process. Another advantage is ability to produce force in two opposite directions; i.e. force and restoring force, which can be used to either close or open the switch more reliable than the other switches. The trade-off for this benefit is that the switch becomes larger in size and slower. One possible actuator for these switches is comb drive actuator. It is noteworthy to say that lateral force switches are not limited to electrostatic actuation, as other types of actuation methods can be used as well [9].
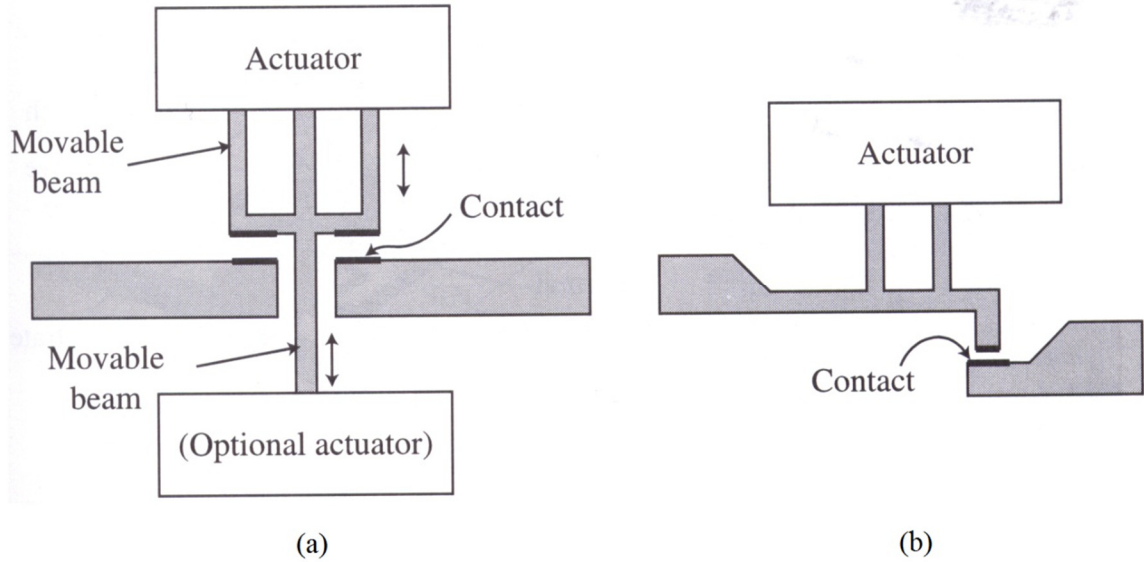
Figure 19: Lateral force switches (a) one-contact and (b) two-contact [9].

2.2.3. Rotary Switches

Although this type of switch is not used anymore, it was one of the first high-performance MEMS switches. An early rotary switch is shown in Figure 20. The operation principle is shown in Figure 21. Having applied a voltage between two facing electrodes, positive and negative charges are induced in rotor causing an attractive force and the rotation of the switch. By switching the voltage to the next electrodes, the rotor can be made to rotate around the anchor [10]. This switch has large mass and is slow (typical maximum rotation speeds are in the tens of kHz). Also, it needs high voltage actuation and is unreliable due to friction in the operation mechanism [9].
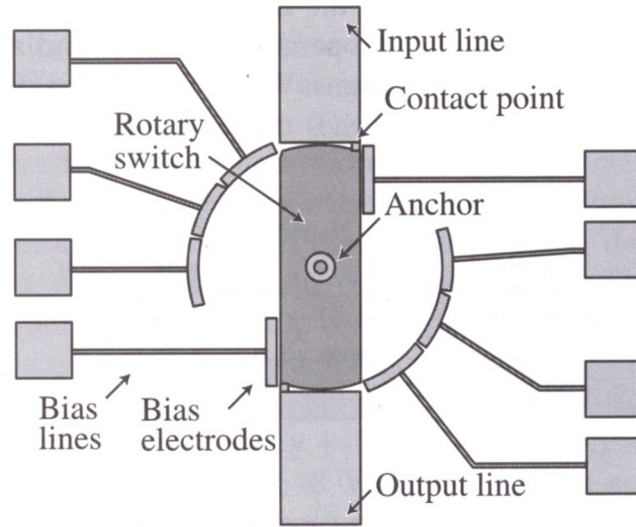
Figure 20: Rotary switch [9] (Copyright IEEE).
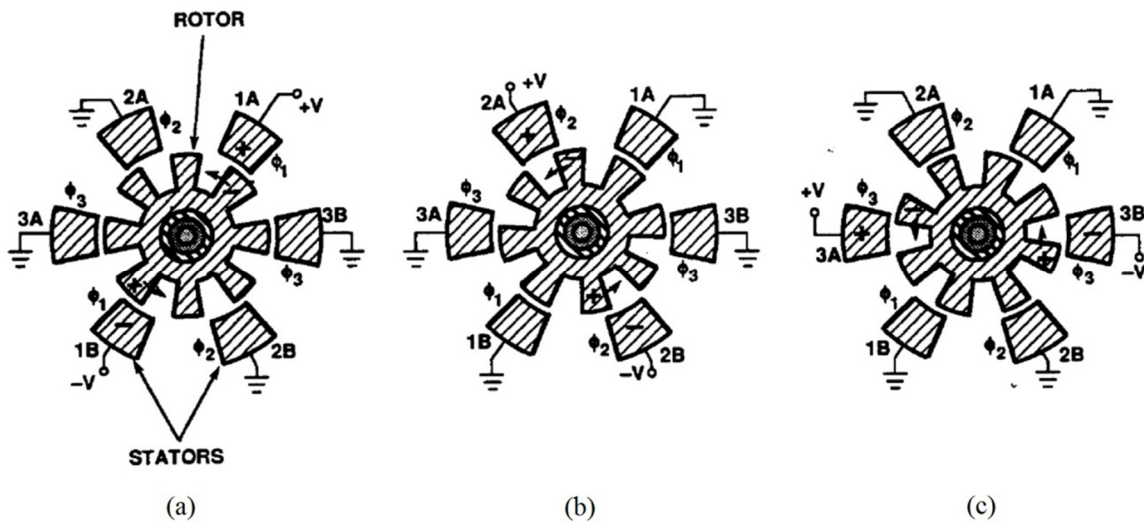
Figure 21: Operation principle of the rotary switch [10] (Copyright IEEE).

2.2.4. Magnetic Actuation

An example of a magnetic actuation switch is shown in Figure 22. This design is appropriate for application in which minimal power consumption is needed such as satellite and portable electronics. Once the switch is actuated and goes to "on" or "off"

state, it can retain that state in absence of applied power. It is also called a latch switch or relay.

When a beam with a length much larger than its width and thickness is placed in a permanent magnetic field, dipoles tend to rearrange along the length and a torque is created on the beam, which can cause rotation if the beam is anchored at its middle. The torque can be either clockwise or counterclockwise depending on the initial orientation of the beam with respect to the magnetic field. If the angle α between the beam and the magnetic field vector is less than 90°, the torque is clockwise, and if α is greater than 90°, the torque is counterclockwise. In order to switch between these two sates, we need to change the direction of the magnetic field. This can be done by means of another magnetic field which can be produced by a coil. We use the new magnetic field only to change the direction, and afterwards the permanent magnetic field can rotate the beam to the opposite state. The coil magnetic field should satisfy the following condition,

$$H_{\xi}^{Coil} \geq H_0 \cos \alpha \tag{6}$$

where $H_{\xi}{}^{Coil}$ is the component of the momentary magnetic field along the beam and H_0 is the permanent magnetic field [9], [11].
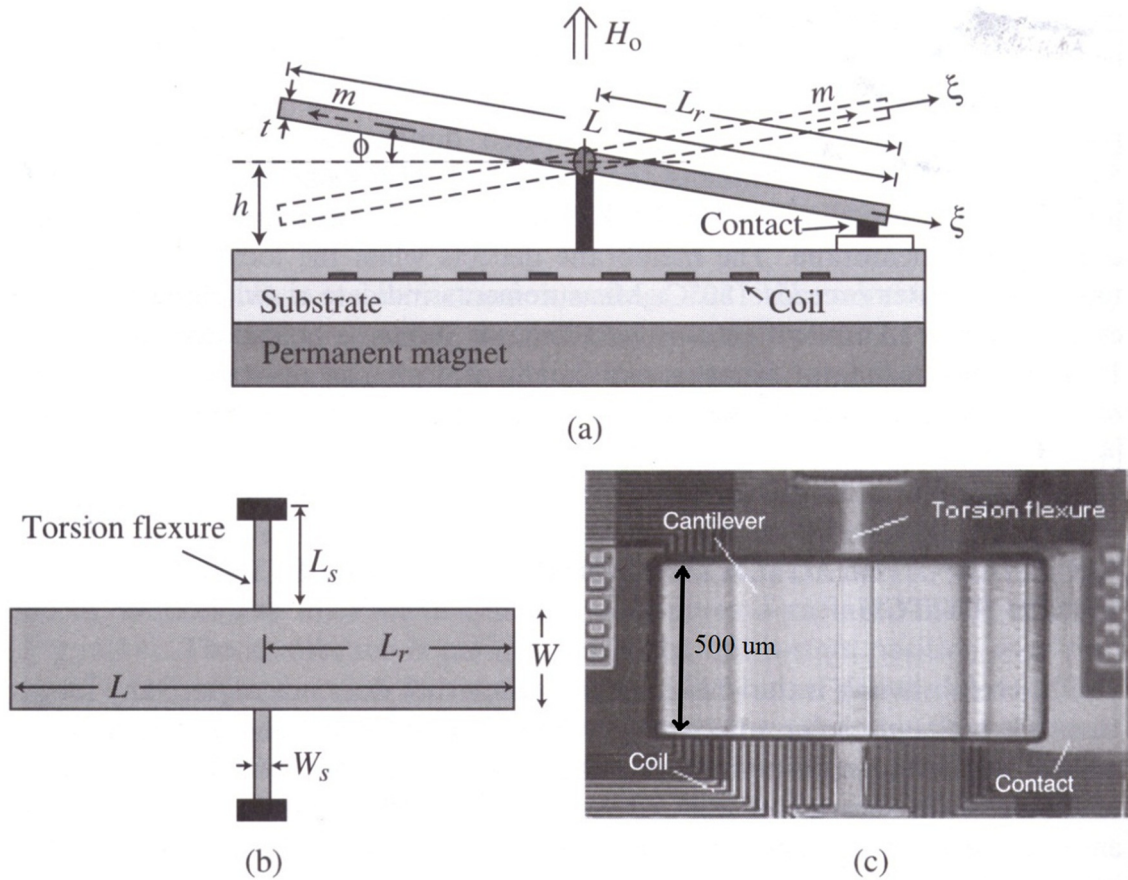
Figure 22: Magnetic switch [9] (Copyright IEEE).

2.2.5. Thermal Actuation

The benefit of electrostatic switches is their low power consumption, however, they usually need high voltages. To decrease the voltage one can take advantage of thermal actuation. In the design of Figure 23, the bridge is pulled down by thermal expansion until it is in the down-state position. Thermal actuation is provided by two resistive heaters. The membrane is made of different PECVD layers with compressive and tensile stresses and is designed to have a vertical stress gradient such that when it is heated, it tends to bend down. Then a DC voltage is applied between the electrodes to keep the membrane down using electrostatic force [9].

26
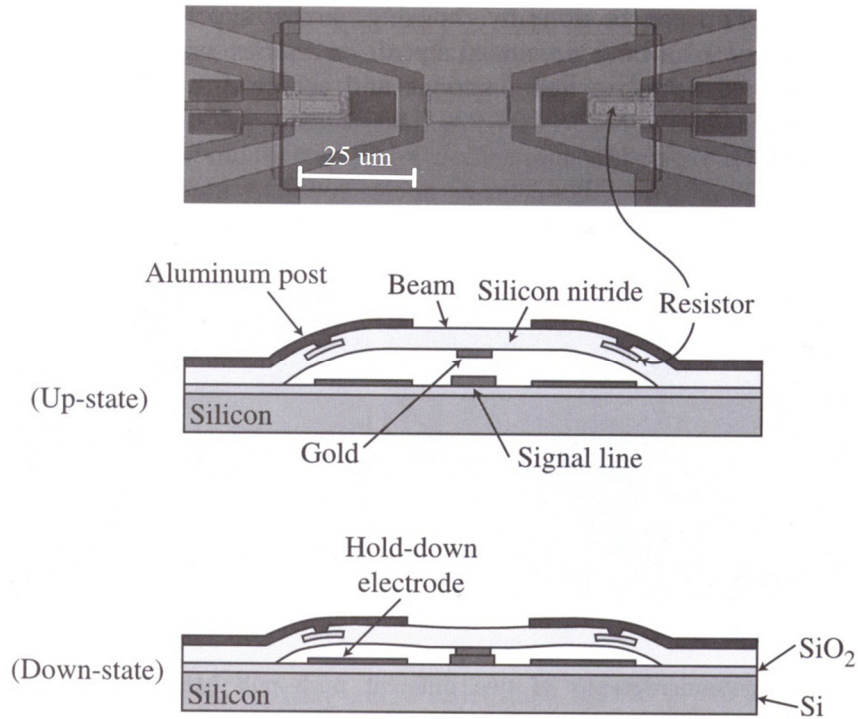
Figure 23: Thermal switch [9] (Copyright IEEE).

2.2.6. Piezoelectric Actuation

Most of the structures discussed in the previous sections could be built using piezoelectric actuation. Piezoelectric actuation requires a layer of piezoelectric material above the structure and at the edges. When a voltage is applied to the piezoelectric material it expands or contracts depending on the polarity of the applied voltage. Therefore, piezoelectric actuation can provide a restoring force which helps against stiction problems. The amount of deflection depends on the piezoelectric material, its thickness, and the applied voltage [9]. One example of this type of switch is shown in Figure 24.
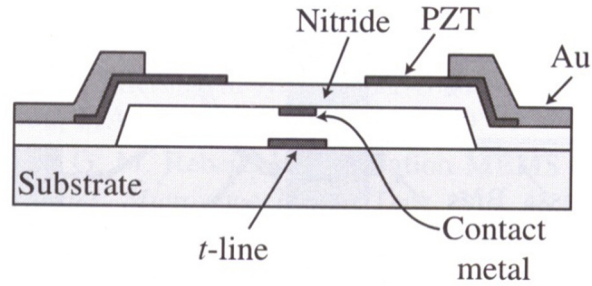
Figure 24: Piezoelectric switch [9]

2.3. Frequency Selective Surfaces

A Frequency Selective Surface (FSS) is a two dimensional periodic array of dipoles, patches, slots, or apertures acting as a reflecting or transmitting surface, which has band-pass filter characteristics [12]. Possible applications include multiband reflector antennas, radomes, absorbers, artificial electromagnetic band gap materials, and optical filters [13], [14].

2.3.1. Principle of Operation

If an FSS is illuminated by incident waves of different frequencies, ideally at one certain frequency the wave reflects off the surface and at the other frequencies the waves pass through the surface, or vice versa. The transmission and reflection coefficients of the two cases are shown in Figure 25.
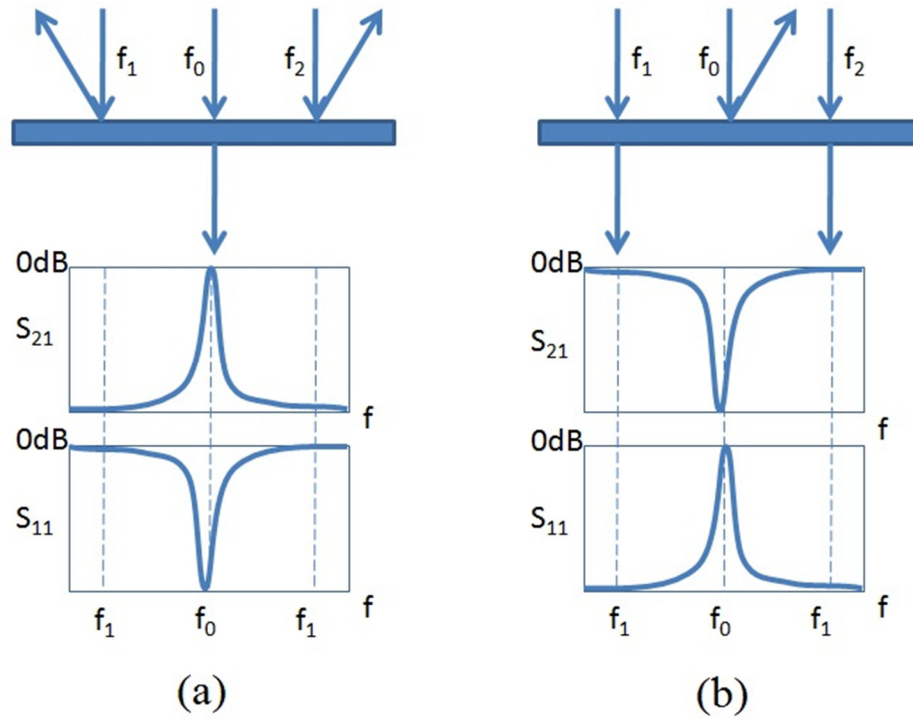
Figure 25: Transmission and reflection coefficients of two different types of FSS.

To explain these phenomena, one can use the equivalent circuit of the FSS. The equivalent circuits of two simple FSS, an array of apertures in the ground plane and an array of patches, are shown in Figure 26.
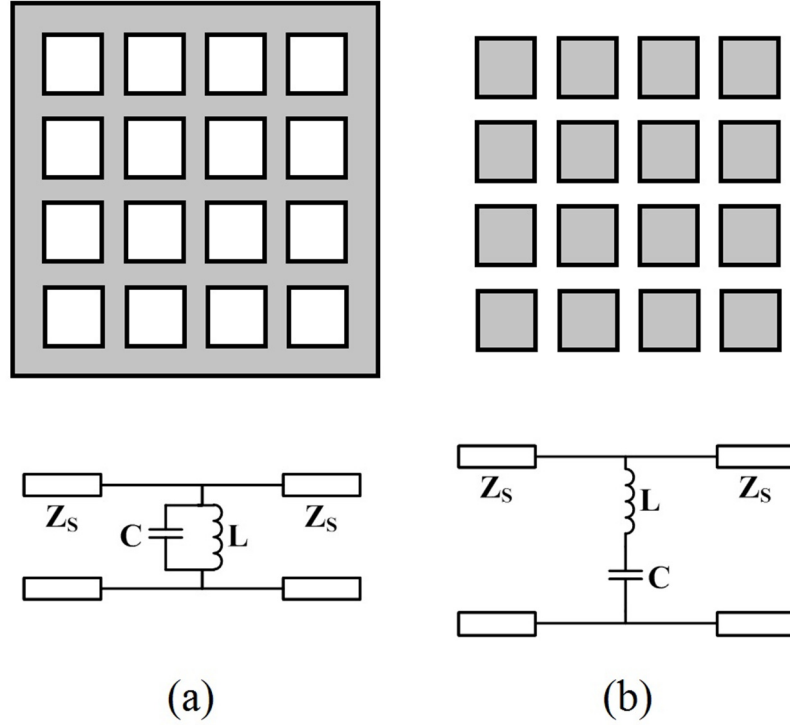
Figure 26: The equivalent circuits of two different types of FSS [15].

For an array of apertures, the equivalent circuit is a parallel resonance circuit, which at the resonance frequency is ideally an open circuit so that the wave can pass through the FSS. For other frequencies, it is a short circuit and the waves reflect off the FSS. The same approach can be used to explain the operation of an array of patches. In this case, the equivalent circuit is a series resonance circuit which at the resonance frequency is ideally a short circuit so that the wave reflects off the FSS. For the other frequencies, it is an open circuit and the waves pass through the FSS [15]. The resonance frequency of the FSS based on its equivalent circuit is:

$$f_0 = \frac{1}{2\pi\sqrt{LC}} \tag{7}$$

where *L* and *C* are the equivalent inductance and capacitance of the FSS.

Another approach to explain the operation of an FSS is by analyzing each component of the array separately. For example for an array of patches, each patch is an antenna which resonates at the frequency where the wavelength equals half the length of the patch. When this frequency is incident on the patch, the wave is re-radiated by the patch, and so it passes through the FSS. For the other frequencies, the patch does not resonate and the wave reflects off. An array of apertures can be explained in a similar way. It is important to mention that the resonance frequency of an FSS is not the resonance frequency of each element. Rather it is the superposition of all the elements, or strictly speaking the scattering of the wave should be considered. This simplifying of the problem helps us to understand the operation of an FSS [16]. The resonance frequency (first mode) of each element based on this approach is:

$$f_0 = \frac{c}{2L_e\sqrt{\varepsilon_e}} \tag{8}$$

where *c* is the velocity of light, L_e is the effective length of the patch considering the fringing effect and ε_e is the effective permittivity of the substrate.

2.3.2. Reconfigurable FSS

It is of our interest to have a reconfigurable FSS. Profound investigations have already been done on the matter demonstrating that the resonance frequency and the bandwidth of the FSS can be controlled by changing the different characteristics of the FSS while in operation. Some of the existing designs are discussed in this section.

31

2.3.2.1. Use of a Ferrite Substrate

A ferrite material can be used as a substrate for an FSS. By using a DC magnetic field and changing the DC bias voltage, the permeability of the ferrite substrate changes, which in turn changes the resonance frequency of the FSS [17].

2.3.2.2. Use of a Liquid Substrate

An FSS can be printed on a substrate with a cavity inside it, which is filled with a liquid. By changing the liquid or its quantity, the effective permittivity of the substrate changes, and therefore, the resonance frequency of the FSS can be tuned [18].

2.3.2.3. Physical Displacement of the Elements

Another method of making a reconfigurable FSS is to use two layers of dipoles or apertures with a dielectric in between. By displacing the layers with respect to each other, the resonance frequency of the FSS can be changed [19].

2.3.2.4. Tilting the Dipoles

In [2], an FSS was made from ferromagnetic freestanding dipoles. When applying an external electromagnetic field, the dipoles tilt, changing their effective length as seen by the wave perpendicular to the FSS. Therefore, changing the resonance frequency of the FSS. Figure 27 shows a magnetic tunable FSS in different positions.

Perspective Profile

Projected Length Parallel to the Supporting Surface (Top View)

Tilt Angle: 0°

(a)

60°

Tilt Angle: 60°

(b)

90°

Tilt Angle: 90°

(c)
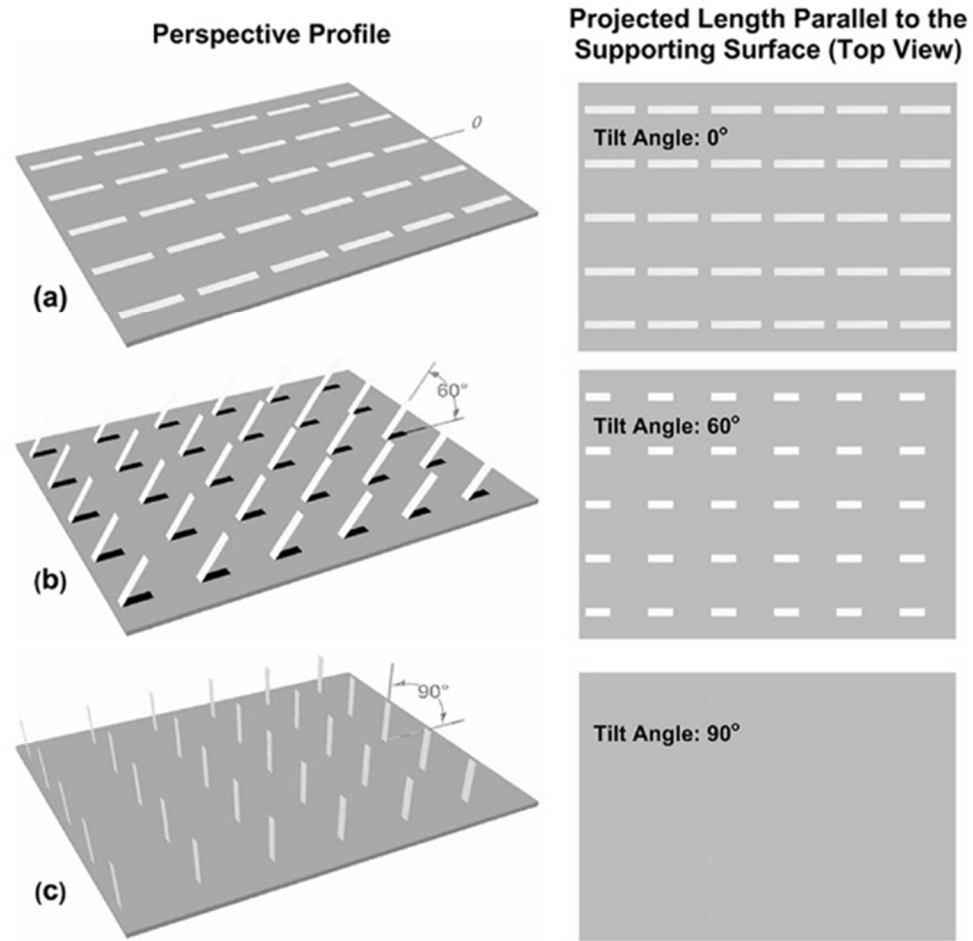
Figure 27: Magnetic tunable FSS [2] (Copyright IEEE).

2.3.2.5. Switching the Dipoles

A switch can be placed between two dipoles such that when it is closed, the two dipoles make a longer dipole, and therefore, changing the resonance frequency of the FSS. A PIN diode can also be placed in the middle of a slot so that it can short the slot and make two smaller slots, and therefore, changing the resonance frequency of the FSS [20], [21].

2.3.2.6. Illuminating the Substrate

In [22], a semiconducting material was used as the substrate for an FSS. By illuminating the substrate, its conductivity changes and therefore the frequency response of the FSS changes.

2.3.2.7. Loading the Elements

Loading dipoles or slots can be done by different methods. Schoenlinner et al. demonstrated a four-legged loaded element with tunable capacitive loading bridges (Figure 1), which provides a tunable resonance frequency for the FSS [1]. Epp et al. successfully incorporated surface mount varactor diodes on an FSS with loop elements to change the resonance frequency [23].

2.3.2.8. Summary

All the above presented frequency selective surfaces have their own disadvantages such as high loss (ferrite substrate, PIN diode, varactor diode), high cost (ferrite substrate, varactor diode), high mass (ferrite substrate), external source (tilting the dipoles, semiconductor substrate), complicated design (liquid substrate, four-legged loaded elements) [1].

An electrostatic MEMS switch can be used to solve the high loss, high cost, high mass and external electromagnetic source problems. This was done in [1] by using a Jerusalem cross loaded by four MEMS bridges at its four corners (Figure 1). Four bias bridges and four islands in the ground plane were used to actuate the MEMS bridges. This method of actuating eliminates the need of a bias line network, however, it makes

the design complicated for fabrication and modeling. In this thesis, complexity problem is

solved by using only one MEMS bridge over a slot. The trade-off is the bias line network

that is used to actuate each MEMS bridge.

Chapter 3

Design and Simulation

3.1. Introduction

Ideally, an FSS is a periodic structure that continues to infinity, however, it is just a hypothetical concept. In practice, a finite two-dimensional array of elements is used to make an FSS, for example 10×10. Such an array scatters the incident wave in such way that only frequencies around a specific resonance frequency are transmitted and the other frequencies are reflected off the surface. Each element of the array is called a cell. The periodical nature of an FSS can be used to reduce the EM analysis of the FSS. In solving EM problems, symmetrical structures can be reduced in size by removing the other similar half and replacing the boundary with a perfect electric conductor (PEC) or perfect magnetic conductor (PMC) depending on the direction of the fields. If the electric field is orthogonal to the boundary, the boundary is replaced by a PEC, and if the electric field is parallel to the boundary, the boundary is replaced by a PMC (Figure 28).
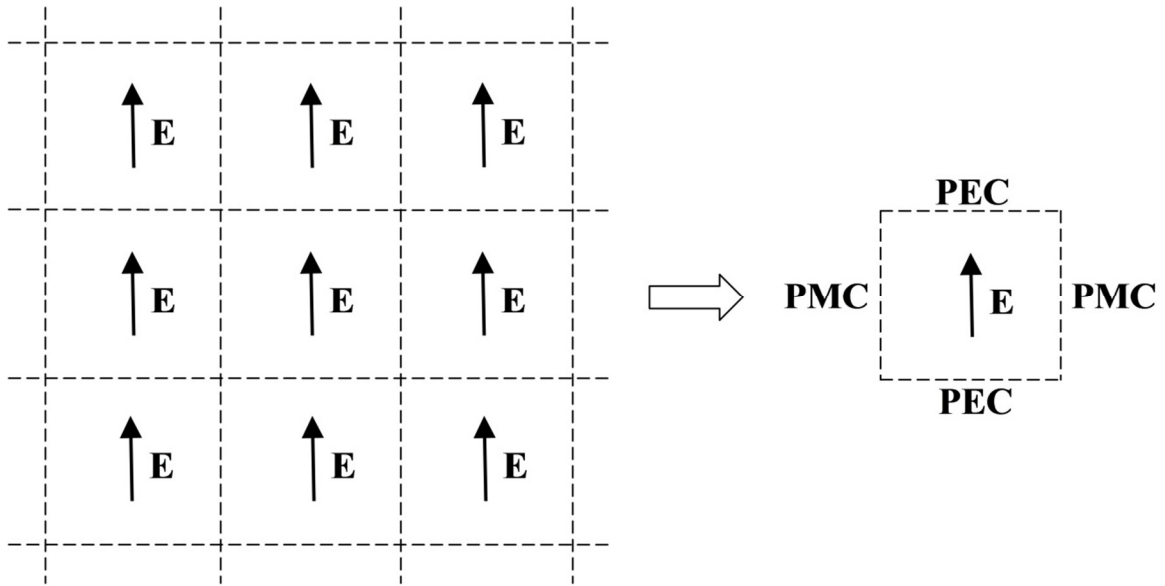
Figure 28: Reducing an infinite periodic structure to one unit cell

This reduction technique can be used to fabricate only one cell instead of the whole array. The difference is that the single cell has to be surrounded by proper PEC and PMC walls. In chapter 2, it was stated that the proposed FSS is based on using slots in the ground plane. According to what was explained above, the proper locations of PEC and PMC boundaries for such cell are shown in Figure 29.
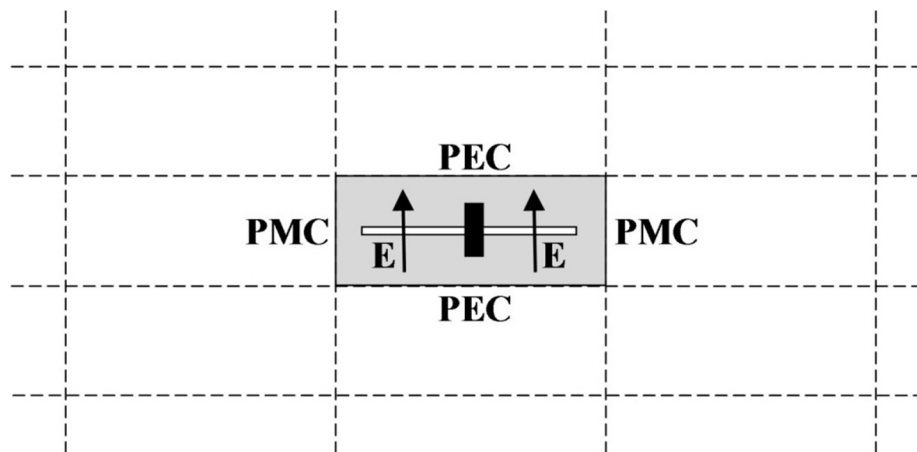
Figure 29: Unit cell configuration

In practice, a good electrical conductor can be utilized as a PEC boundary, but fabricating PMC boundary is difficult and can itself be a separate project. A waveguide is used to solve this problem. The polarization of the wave in a waveguide is linear and along the smaller side, therefore, even though it has four PEC boundaries, it can provide the same field condition as the case with two PEC and two PMC boundaries. There will be a slight shift in a resonance frequency of the FSS when testing with a waveguide compared to testing the entire array, due to the fact that the electric field is perpendicular to all the walls of the waveguide. In Chapter 5, the frequency response of the fabricated FSS will be measured in an X-band waveguide and the results will be compared with the HFSS simulation with four PEC boundaries to account for the shift in the resonance frequencies.

3.2. Design of the Cell and MEMS Bridge

The purpose of this project was the design and fabrication of a tunable FSS, therefore, different structures were tried using Ansoft HFSS. This process took me about six months, during which I examined different ideas of how to change the resonance frequency of an FSS. Different periodic structures were designed which can be categorized into two main categories: an array of patches, and an array of holes in the ground plane (Figure 26). Eventually, an FSS based on slots in the ground plane with a MEMS bridge over the slot was designed (Figure 31).

The idea is that the MEMS bridge over the slot forms a capacitor which is in parallel with the equivalent capacitor (Figure 26 (a)) of the FSS. Therefore, the equivalent circuit of a slot based FSS with a MEMS bridge over the slot has another capacitance caused by

the bridge (C_m) in parallel with C, which is shown in Figure 30. The resonance frequency of the FSS is described as follows:

$$f_0 = \frac{1}{2\pi\sqrt{L(C + C_m)}} \tag{9}$$
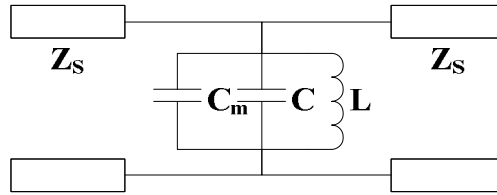
Figure 30: The equivalent circuit of a slot based FSS with a MEMS bridge.

Therefore based on the Equation 11, the resonance frequency of the FSS can be changed by changing the capacitance between the MEMS bridge and the ground plane. The capacitance caused by the MEMS bridge can be changed by changing the height of the MEMS bridge, which in turn can be done by applying a voltage to the MEMS bridge with respect to the ground plane. The electrostatic force caused by the applied voltage bends down the MEMS bridge and increases the equivalent capacitance of the FSS ($C+C_m$).

The advantages of the structure are:

1. The MEMS bridge could provide a significant shift in frequency.
2. The electrostatic actuation method is more common.
3. The MEMS bridge uses the ground plane as the pull-down electrode, therefore, the design eliminates the need for an extra pull-down electrode.

4. Although the same concept was used by Schoenlinner et al. in Figure 1, the advantage of the proposed design in this thesis is that the design uses only one MEMS structure and also it does not use bias bridges, which makes the fabrication process easier.

The disadvantage is the need for a bias line network (compared to the design in Figure 1). The bias line network is a set of lines that connect the actuation voltage to each MEMS bridge.
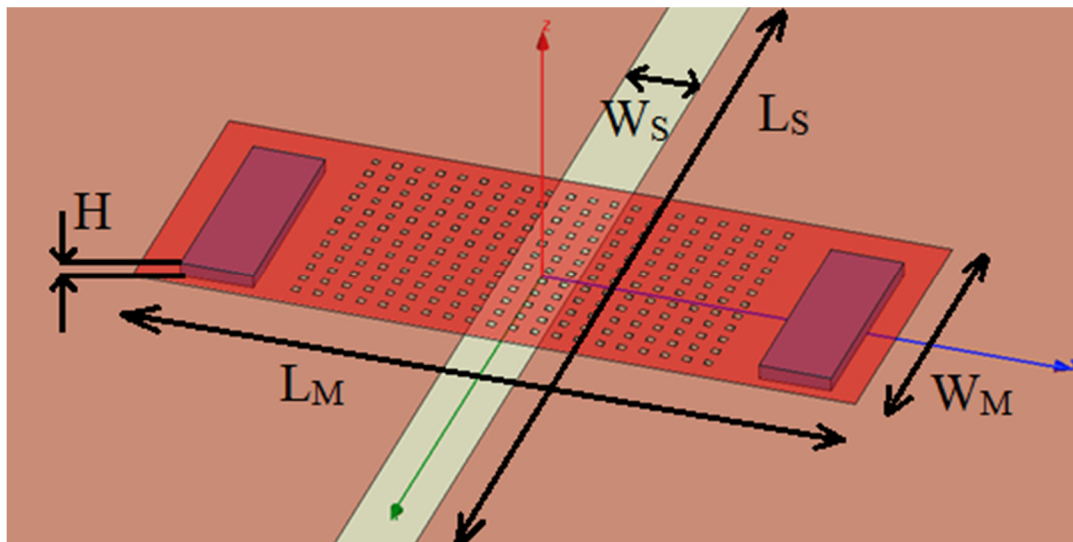
Figure 31: MEMS bridge over a slot.

3.2.1. Choosing the Dimensions of the FSS

An X-band waveguide was used to test the designed FSS because of the availability of both the waveguides and the waveguide-to-coax adaptors. The X-band waveguide dimension is 0.4 in × 0.9 in. Therefore for a slot in the ground plane without a substrate, the length of the slot (L_S) has to be between 0.4 and 0.9 in, so that the resonance frequency of the FSS falls in the X-band frequency range (8.2-12.4 GHz). Quartz

(GE124) was chosen as a substrate due to less power loss and cheap price. The permittivity of quartz is 3.78 F/m. Reflection coefficients of frequency selective surfaces with different slot lengths are shown in Figure 32. The width of the slot is 50 µm. The criteria to choose the width of the slot are also discussed in this section. Ansoft HFSS was used to obtain the reflection coefficients. The length of 8 mm was chosen since it is closer to the end of the X-band frequency range and provides a wider range to decrease the resonance frequency by capacitive load (MEMS bridge).
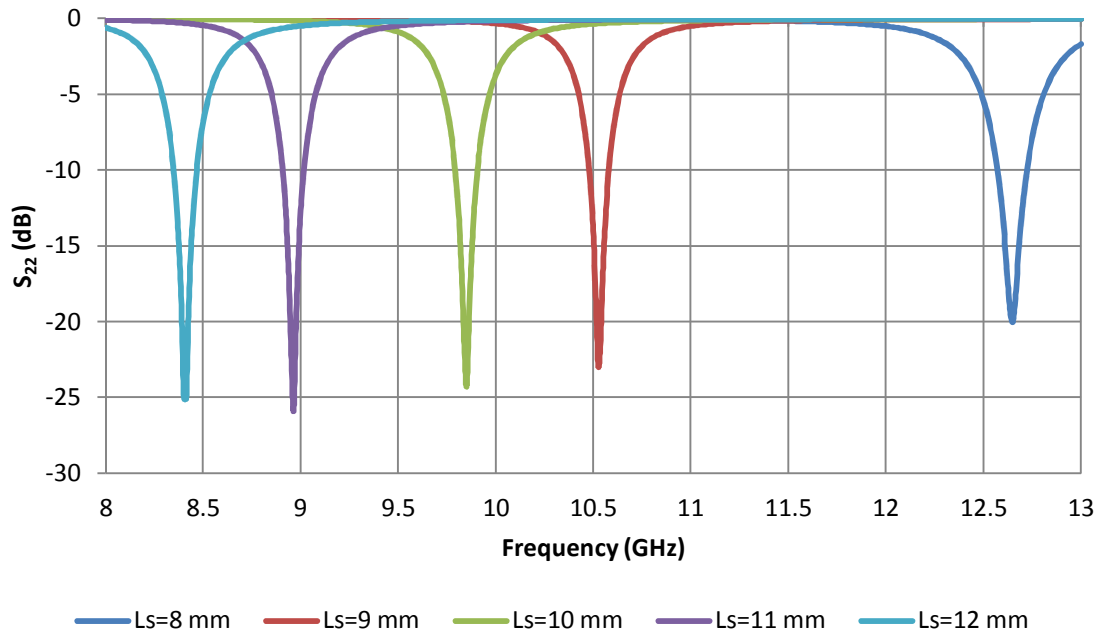
Figure 32: Simulated reflection coefficients for different slot lengths.

The width of the slot does not have a noticeable effect on the resonance frequency of the FSS since the resonance frequency is the first mode which depends on L. Figure 33 shows the reflection coefficients of frequency selective surfaces with different widths of the slot. The criteria to choose W is the size of the actuation electrodes. In fact, there is no actuation electrode but the overlapping area between the ground plane and the MEMS

41

bridge. Therefore the larger the width of the slot is, the smaller the overlapping area will be. W_S was chosen to be 50 µm, therefore, the size of each presumed actuation electrode is 200 µm × (300-50) / 2 µm. The other advantage of a 50 µm wide slot is that the bandwidth of the reflection coeffcient is smaller.
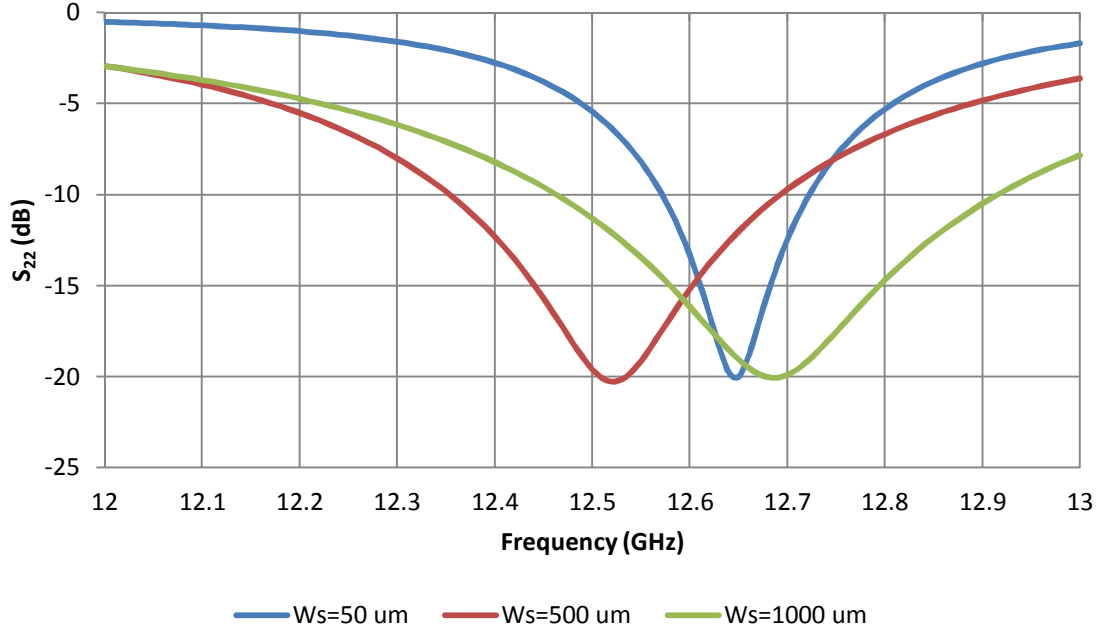
Figure 33: Simulated reflection coefficients for different slot widths.

3.2.2. Choosing the Dimensions of the MEMS Bridge

The width, length, and height of the MEMS bridge define the ability of the tunable FSS to shift the resonance frequency. Any frequency shift should not be too much so that the resonance frequency exceeds the X-band frequency range. Ansoft HFSS was used to examine different combinations of the three variables W_M, L_M, and H. Figure 34 shows how the resonance frequency decreases by fixing W_M at 200 µm, H at 4 µm, and increasing L_M. The same trend follows by fixing L_M at 500 µm and, H at 4 µm, and increasing W_M in Figure 35. In fact, it is the surface area of the MEMS bridge ($W_M \times L_M$)

that can change the resonance frequency of the FSS. A 200 µm × 300 µm MEMS bridge with the height of 4 µm was chosen since its resonance frequency occurs at the end of the X-band frequency range. The effect of the height of the MEMS bridge will be discussed in the Section 3.4. An issue is that a sacrificial layer is necessary to fabricate a MEMS bridge. A sacrificial layer is basically a temporary layer that is deposited to keep the bridge in the up position during bridge fabrication. After bridge fabrication, it is removed partially so that the MEMS bridge can stand on its anchor points located at the two ends of the bridge that were not etched. A more detailed description of the fabrication process is discussed in Chapter 4. The height of the sacrificial layer is limited by the method of deposition. For example, depositing a 1 mm thick layer of silicon with sputtering system is not possible due to stress in the silicon array. Also, a higher H results in a higher actuation voltage. COMSOL Multiphysics was used to determine the actuation voltage needed to deflect the MEMS bridge, which will be discussed later in this chapter.
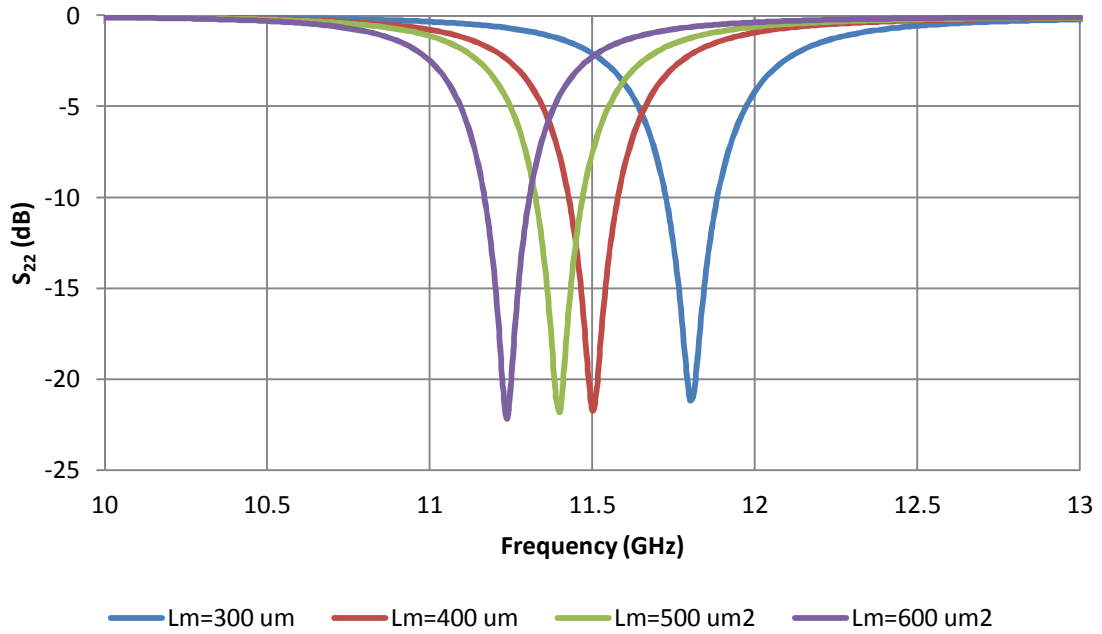
Figure 34: Simulated reflection coefficients for different lengths of the MEMS bridge (W_M=200 µm, H=4 µm).
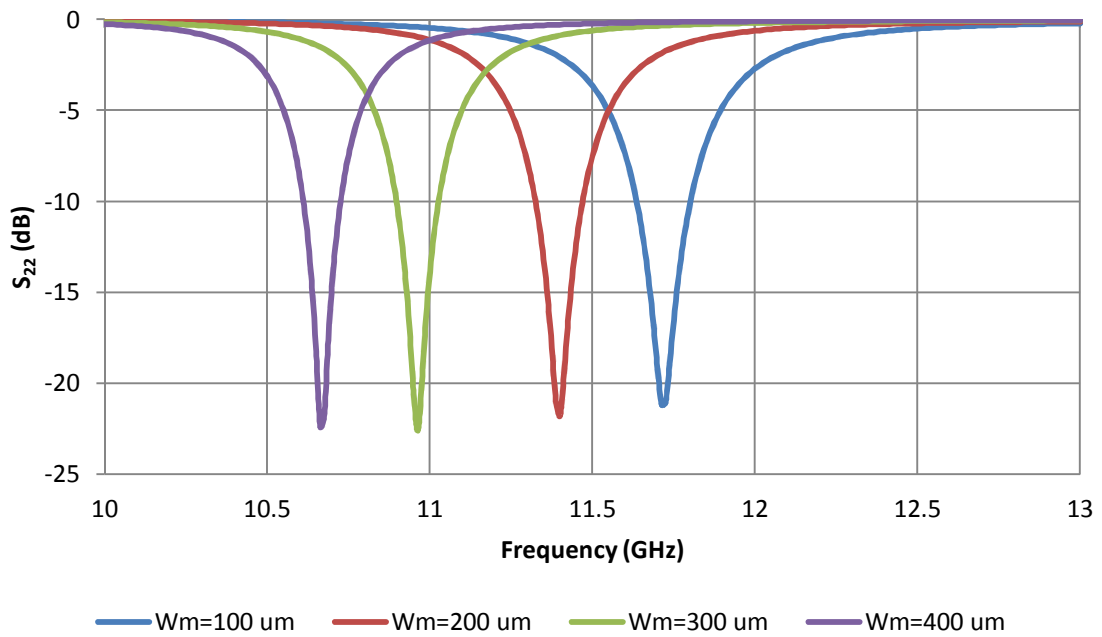
Figure 35: Simulated reflection coefficients for different widths of the MEMS bridge (L_M=500 µm, H=4 µm).

44

Another parameter is the thickness of the MEMS bridge. There are two important requirements that have to be met. First, the thickness of the MEMS bridge should be more than the penetration depth of the EM wave in X-band frequency, so that the MEMS bridge can operate properly as a capacitive load. Second, a snap-shut voltage of about 30-50 V is desirable for the MEMS bridge, in order to operate within common voltages used in satellite communication, which do not exceed 80 V. The penetration depth can be calculated from the following equation:

$$\delta = \frac{1}{\sqrt{\pi f \mu_0 \mu_r \sigma}} \tag{10}$$

where f is the frequency of the wave, μ_r is the relative permeability of the metal layer, and σ is the conductivity of the metal layer. According to the Equation (10), the penetration depth for the aluminum layer and the designed resonance frequency 9.64 GHz is 0.77 µm, therefore the thickness of the MEMS bridge is chosen 1 µm.

In Figure 31, holes can be seen on the MEMS bridge. The holes on the bridge help the etchant go under the bridge and etch the underlying sacrificial layer, releasing the bridge. The holes are 5 µm × 5 µm and the spacing between them is 5 µm.

3.2.3. Choosing the Materials for the FSS and MEMS Bridge

There were a few choices of metals available to fabricate the MEMS bridge; copper, aluminum, gold, tungsten, and titanium. Tungsten and titanium are not desirable due to high stress of the material. The problem with gold is that it is expensive. Copper does not stick to the layer below and above it, therefore, it has to be encapsulated between two thin

layers of titanium, which makes the fabrication process longer. The best choice is aluminum and this was selected as the material for the MEMS bridge and also the ground plane.

After fabrication, the aluminum ground plane is coated with a 100 nm silicon dioxide layer in order to electrically insulate the MEMS bridge from the ground plane when the bridge is in down position. Silicon dioxide was chosen due to high dielectric strength. The thickness of the oxide layer is calculated from the following equation:

$$t_{SiO_2} > \frac{Break\text{-}down\ voltage\ needed}{Dielectric\ stregth\ of\ SiO_2} = \frac{Snap\text{-}shut\ Voltage}{Dielectric\ stregth\ of\ SiO_2} \qquad (11)$$

where the *Dielectric strength of SiO₂* is 1 V/nm, and desired *Snap-shut voltage* is 40 V, therefore, the thickness of SiO_2 should be greater than 40 nm.

3.2.4. Summary of the Design

A summary of the proposed design is shown in Table 1.

Table 1: Summary of different parameters in the proposed design.

Material used for the substrate	Quartz (GE124)
Material used for the ground plane	Aluminum
Width of the slot	50 μm
Length of the slot	8 mm
Width of the MEMS bridge	200 μm
Length of the MEMS bridge	300 μm
Initial height of the MEMS bridge	4 μm
Thickness of the MEMS bridge	1 μm
Material used for the MEMS bridge	Aluminum
Thickness of the insulator layer	100 nm
Material used for the insulator layer	SiO_2

3.3.   Electro-Mechanical Analysis

COMSOL Multiphysics 3.5a was used to carry out the electromechanical analysis. Three modules Solid Stress-Strain, Moving Mesh (ALE) and Electrostatics were used for simulation. Static analysis types were selected for the modules. Aluminum and silicon were assigned as the materials for the bridge and the posts, respectively. The COMSOL model of the MEMS bridge is shown in Figure 36.
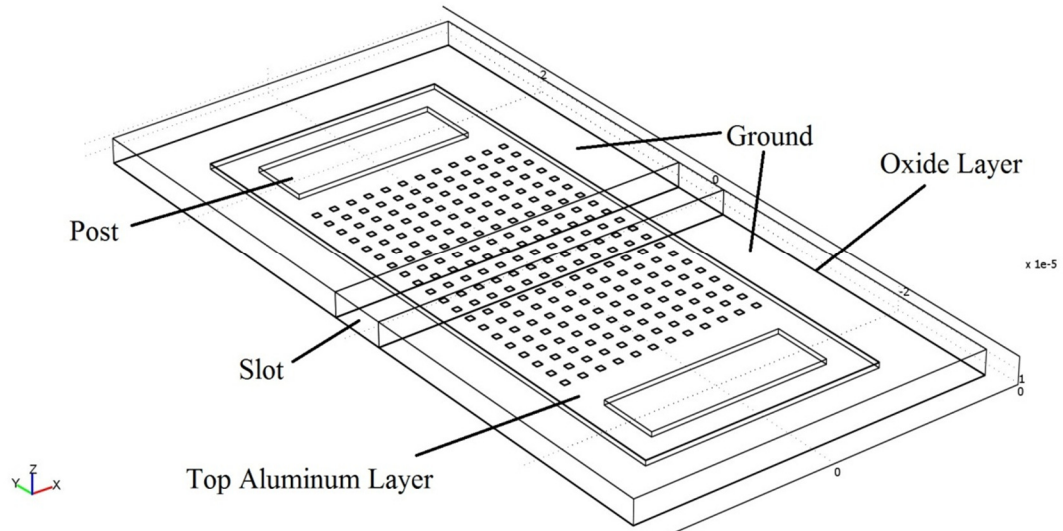
Figure 36: COMSOL model of the MEMS bridge.

The dimensions and specifications of the MEMS bridge were discussed in the last section. The oxide layer is too thin (100 nm) to be seen in Figure 36. The ground boundary conditions were assigned to the bottom surface of the oxide layer, except where the slot is located. The variable V_{in} boundary condition was assigned to the bottom surface of the top aluminum layer, except where the holes are located. Therefore, the distance between the top aluminum layer with the V_{in} voltage and the ground is 4 µm (the height of the posts) + 100 nm (the thickness of the oxide layer) = 4.1 µm.

COMSOL Multiphysics is based on finite element method (FEM). In FEM, one important issue is the number of meshes which determines the accuracy of the model. For the solution to be valid, a minimum number of meshes is required. To find the minimum number of meshes, one can start from a low number of mesh elements and calculate the solution, then gradually make the mesh finer and check the solution. If the solution does not change significantly after several trials then the last trial can be considered as a good final solution. For this thesis, the mesh consists of 86220 elements. Two more cases;

121656 elements, and 240778 elements were also tried with almost the same results. Therefore, the first meshing was chosen for the simulation since it requires less time to finish the simulation process. Figure 37 shows the mesh.
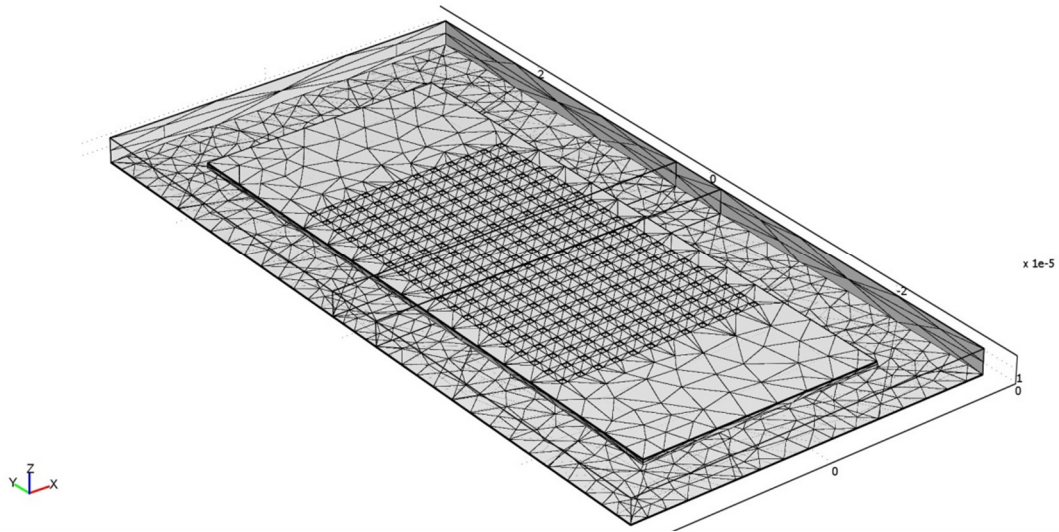
Figure 37: MEMS bridge mesh in COMSOL.

To show that the MEMS bridge changes its position with different applied voltages V_{in}, a color plot of the MEMS bridge at the actuation voltage 39.9 V is shown in Figure 38. Figure 39 shows the cross section of the MEMS bridge for different applied voltages. It can be seen from Figure 39 that the deflected bridge is flat at its middle predicting the bridge tends to bend mostly at its edges. Figure 40 shows the bridge deflection at its middle for different voltages. The snap-shut voltage occurs at 39.9 V. The snap-shut voltage is the voltage at which the bridge becomes unstable and pulls down to the oxide layer. The change in the deflection vs. voltage is more linear at the lower voltages and it becomes non-linear close to the snap-shut voltage.
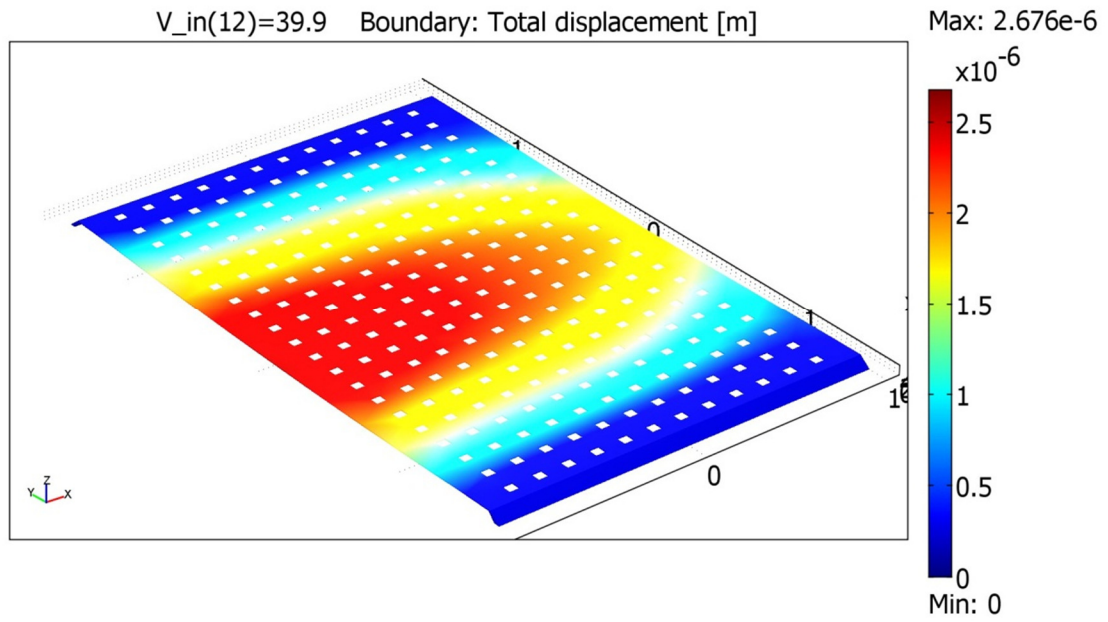
Figure 38: Displacement of the MEMS bridge at the actuation voltage V_{in}=39.9 V.
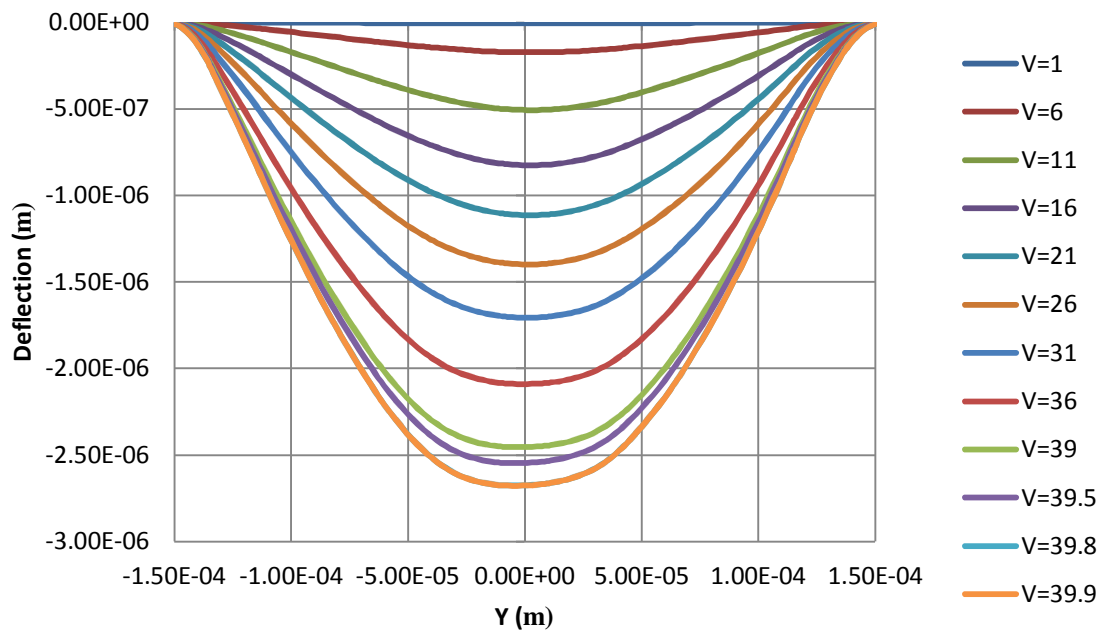
Figure 39: MEMS bridge profiles for different actuation voltages.
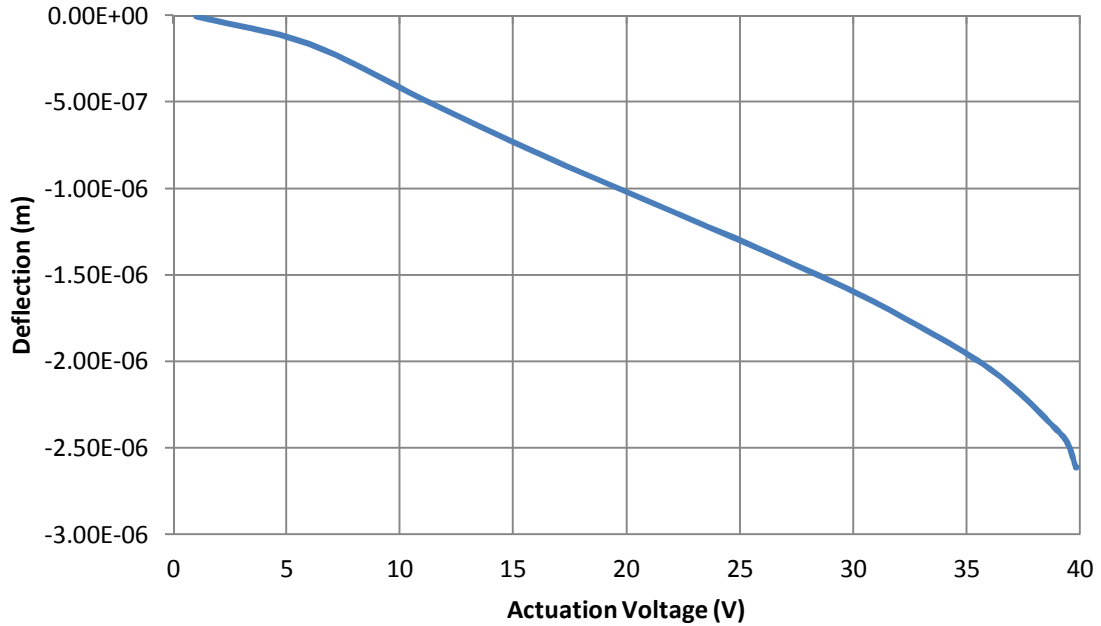
Figure 40: Deflection of the MEMS bridge at its middle vs. actuation voltage.

3.4. EM Analysis

Ansoft HFSS 11 was used to obtain scattering parameters of the FSS. An infinite periodic structure was modeled using PEC and PMC boundaries which were placed orthogonal and in parallel with electric field direction, respectively. The unit cell configuration is shown in Figure 29. The PEC and PMC boundaries were placed orthogonal and parallel to electric field as it was explained in Section 3.2. Ansoft HFSS has an automatic meshing system. It does not offer a manual meshing, therefore, the user does not have many parameters to change the mesh. To show that the FSS operates properly, the frequency response in X-band frequency range has to be investigated. The reflection coefficients (S_{22}) for different bridge deflections are shown in Figure 41.
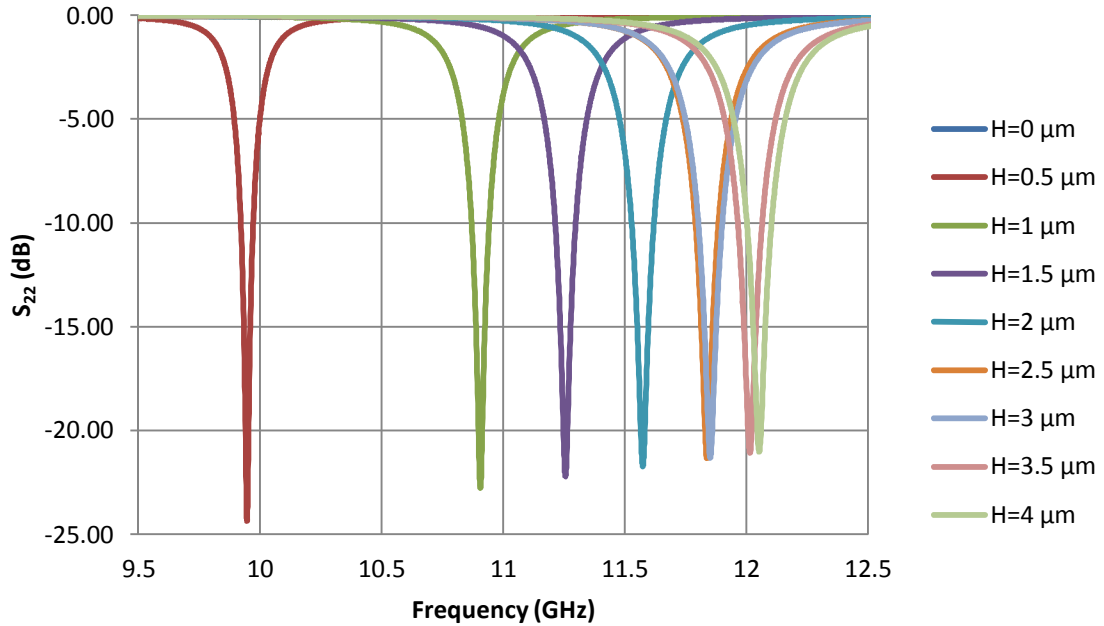
Figure 41: Reflection coefficient for different bridge deflections.

It can be seen that by decreasing the height of the bridge, the resonance frequency shifts lower covering a wide frequency range. Also, the notches are closer together at the high frequencies, and as they move towards the lower frequencies, their separations become more which indicates a non-linear trend. The resonance frequency of an 8 mm long slot is near to the end of the X-band waveguide frequency range (12.4 GHz). This allows us to change the resonance frequency a wide range. It is noteworthy to mention that practically we can only have the resonance frequencies in the range about 11 - 12 GHz which correspond to the deflections 0 - 2.5 µm, because after a deflection of 2.5 µm (snap-shut point) the MEMS bridge becomes unstable and its deflection cannot be controlled by the actuation voltage V_{in}.

The configuration of the cell in Figure 29 is based on two PEC and two PMC boundaries. However, as it was described in Section 3.3, a more realistic way of

modeling a unit cell tested in a waveguide is to assign four PEC boundaries to the walls of the unit cell. The result is shown in Figure 42. It can be seen that when modeling with all PEC boundaries, there is a shift of about 400 MHz in resonance frequencies compared to the previous method in Figure 41. Also, the bandwidth increases.
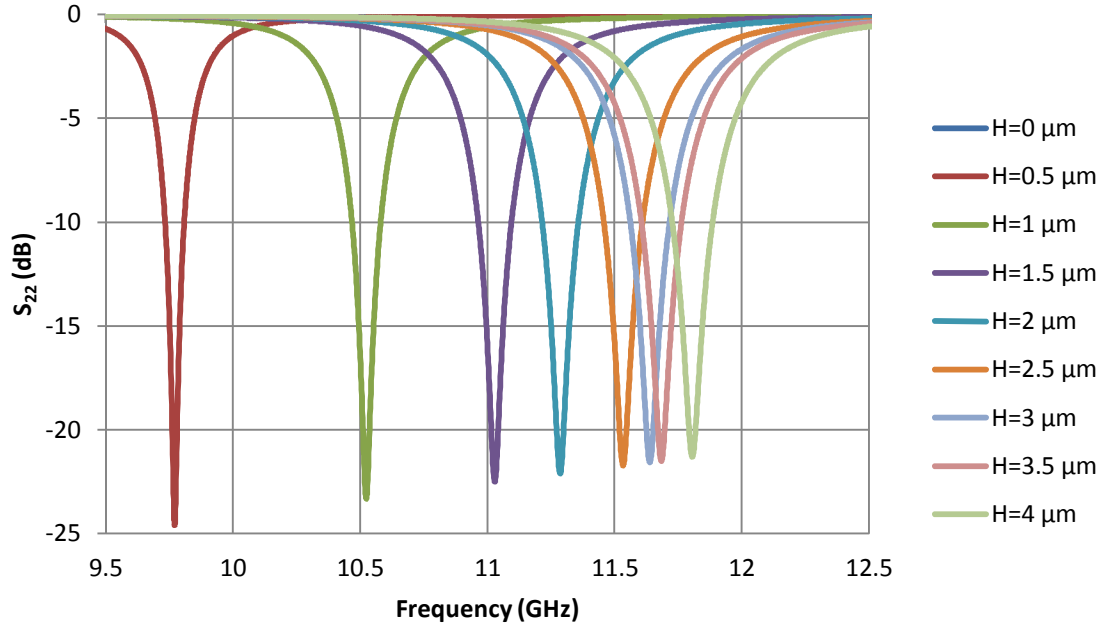
Figure 42: Reflection coefficient for different bridge deflections. All boundaries are PEC.

Chapter 4

Fabrication

The goal is to fabricate a MEMS bridge over a slot in a ground plane as described in Chapter 3. The structure consists of four layers with one layer being sacrificial; therefore three lithography masks were designed and used throughout the fabrication. The masks were fabricated at the NanoFab Facility, University of Alberta. The fabrication process is explained in chronological order. Figure 43 shows the fabrication process and the corresponding masks. In the rest of this chapter, the fabrication process is arranged into different steps, each explaining the materials, techniques, and recipes used to fabricate one layer of the device. The final device is made of four layers.

Deposit and pattern
the first Al layer

Al

Quartz

Deposit and pattern
the oxide layer

SiO$_2$

Deposit the sacrificial layer

Si

No Mask

Deposit and pattern
the second Al layer

Al

Etch the sacrificial layer

No Mask
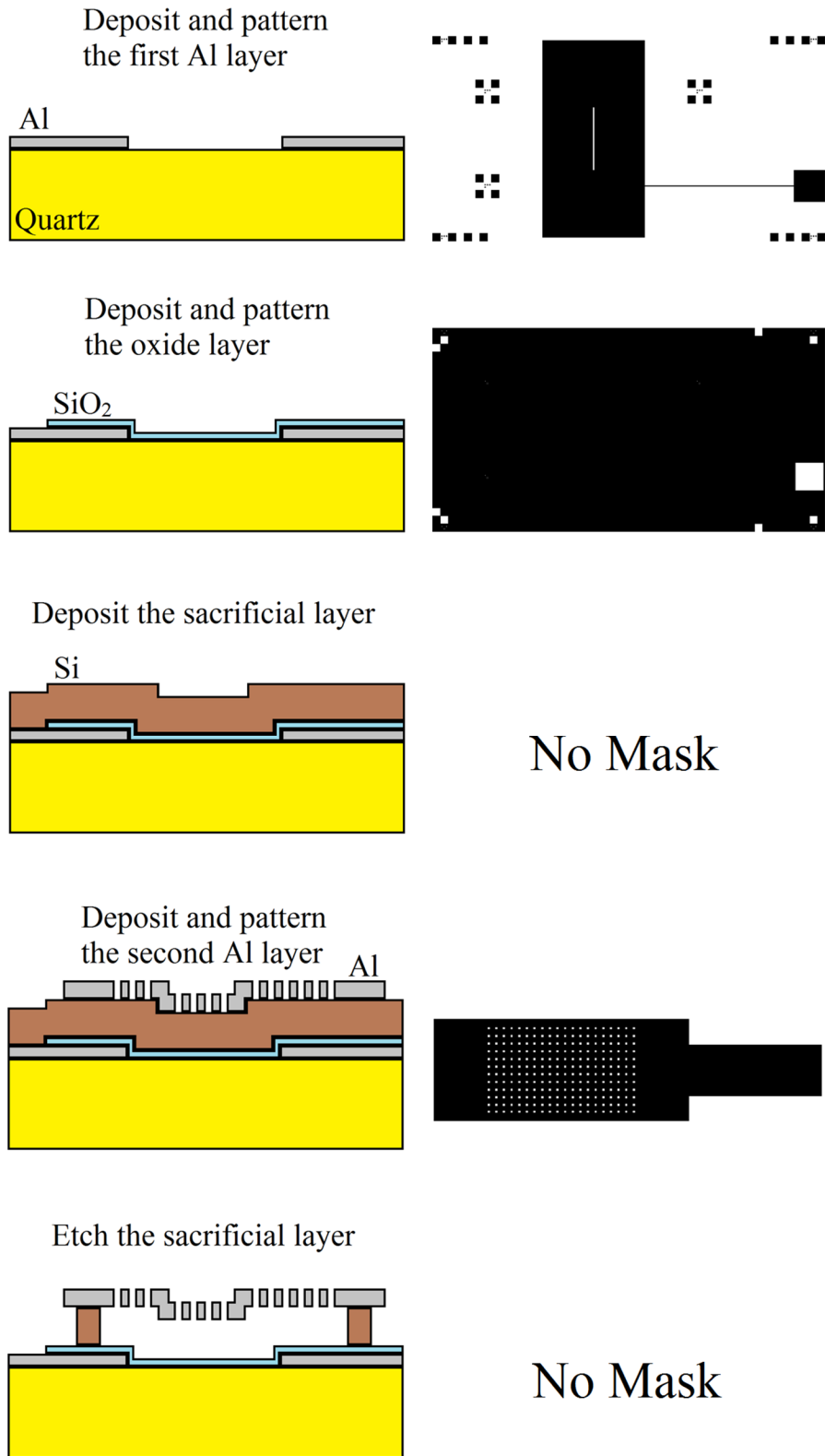
Figure 43: Fabrication process.

55

The ABM mask aligner at the NSFL was used to transfer the pattern from the masks onto the photoresist. Two different types of alignment marks were used to align the substrate to the masks. Some of the alignment marks are 1 mm × 1 mm squares used for rough alignment, others are small crosses used for precise alignment. Examples of the alignment marks are shown in Figure 44 and Figure 45.
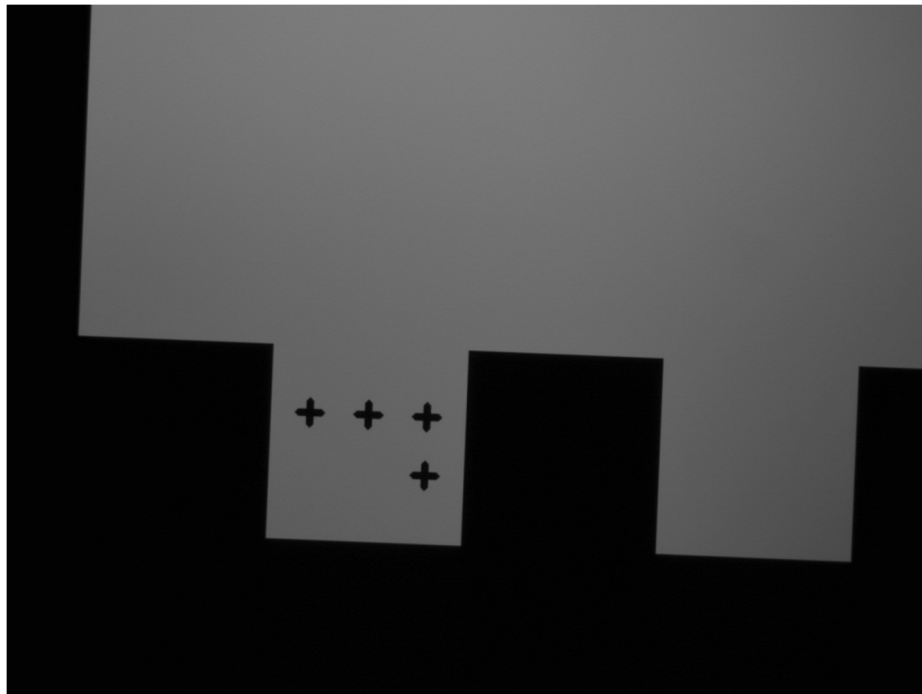
Figure 44: Square alignment marks for rough aligning.
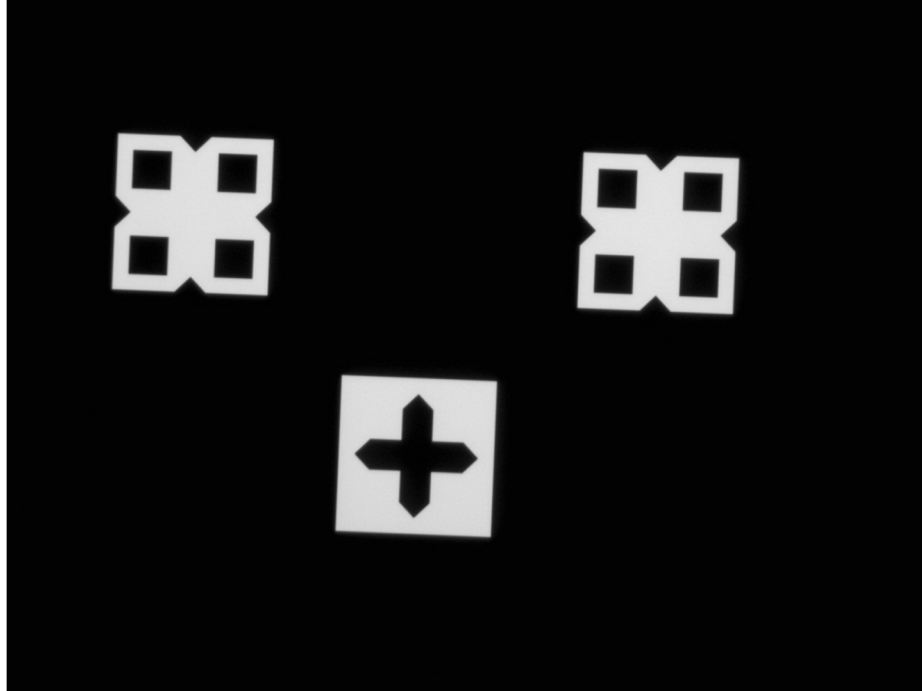
Figure 45: Cross alignment marks for precise aligning.

4.1. Ground Layer

Quartz (GE124) is used as the substrate. The quartz substrate has to be cleaned so that the deposited layer can stick to it firmly. A piranha etch solution ($H_2SO_4+H_2O_2$, 5:1) is used to clean the substrates. The substrate remained in the solution for 5 minutes followed by 5 minutes rinse with deionized water.

The first layer of the structure is the aluminum ground plane which contains the FSS element along with the bias lines. Sputtering method is used to deposit a 1 μm thick aluminum layer on the quartz substrate. The main reason to use sputtering was the better adhesion compared to evaporation of aluminum. The recipe used to sputter aluminum is given in Table 2.

Table 2: Recipe for aluminum sputtering.

Base pressure	6.6×10^{-6} mTorr
Sputter pressure	9×10^{-3} mTorr
Argon flow	64.5 sccm
DC power	200 W
Time	15 min
Thickness	1 μm

This recipe was selected between three trials with three different DC powers; 100 W, 200W, and 300 W. For the case of 300 W, the color of the aluminum layer was white, indicating a high surface roughness. The color of the deposited aluminum layer for 100 W and 200 W were both silver-gray, indicating a smoother surface. The recipe with DC power of 200 W was selected, because the surface was smoother compared to DC power of 300 W and the sputtering time was shorter compared to the DC power of 100 W.

The next step is lithography. The designed mask for the ground plane is shown in Figure 46. The recipe for the lithography is given in Table 3. The bias line and the pad at its end are to connect the ground of the FSS to the ground of the DC power supply. The width and length of the ground are each 1 mm bigger than the width and length of the X-band waveguide. The 1 mm offset is to make sure that the walls of the X-band waveguide (PEC boundaries) make contact with the ground plane. Figure 47 shows the position of the X-band waveguide walls with respect to the ground of the FSS.
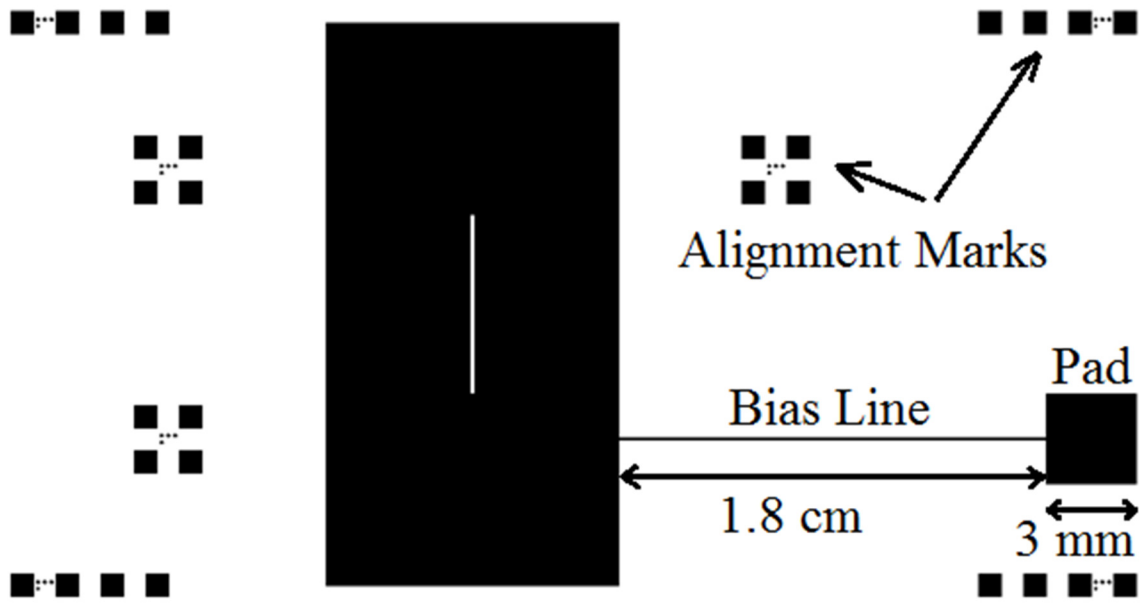
Figure 46: Designed mask for the ground plane.

Table 3: Recipe for lithography.

Spinning speed	5000 rpm
Thickness	1.2 μm
Baking in the oven	30 min at 110 °C
Exposure time	4 sec
Developing time	20 min
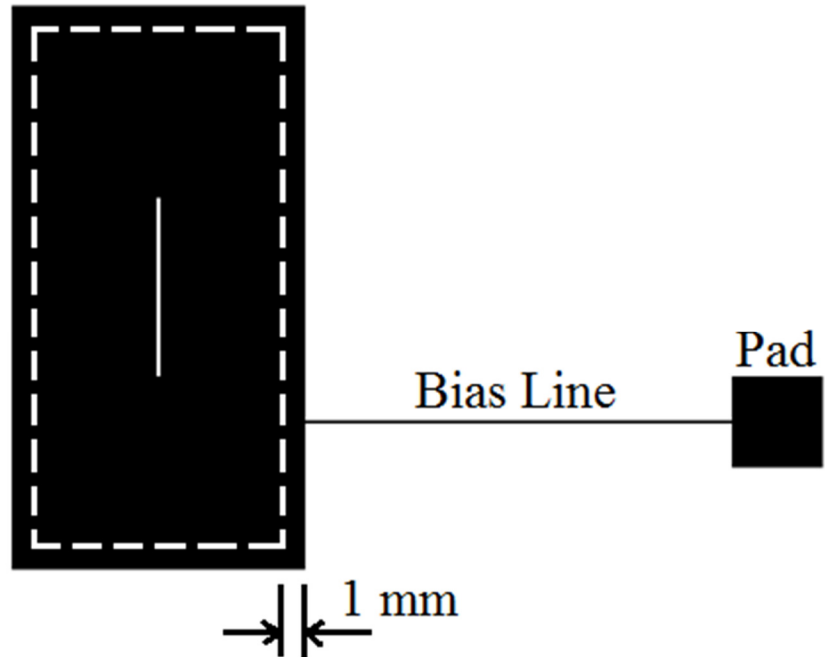
Figure 47: The walls of the X-band waveguide with respect to the ground.

Other recipes with different spinning speeds; 2500 rpm, 3000 rpm, 3500 rpm, and 4000 rpm were tried. The spinning speed of 5000 rpm was chosen because it is high enough to give a uniform spread photoresist on the substrate. One of the common problems in lithography is that photoresist can accumulate at the edges of the substrate during spin coating. The thicker photoresist at the edges will not be removed properly during developing, leaving a ring of photoresist. This will result in incomplete aluminum etching, leaving aluminum at the edge of the quartz substrate, which shorts the ground plane to the top aluminum layer. The high photoresist spinning speed at 5000 rpm solved this potential problem.

The recipe used to etch the aluminum is given in Table 4. The aluminum etch has to be heated up so that it etches the edges of the features sharply. After etching the

60

aluminum layer, the photoresist is removed using acetone. The schematic of the fabricated device up to the first layer is shown in Figure 48.

Table 4: Recipe for aluminum etching.

Etchant	Aluminum etch
Temperature	60 °C
Time	90 sec
Thickness	1 µm
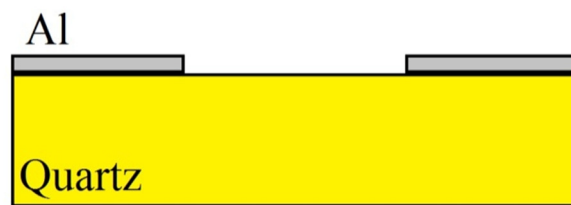
Figure 48: Deposit and pattern the first aluminum layer.

4.2.   Oxide Layer

The oxide layer is used to electrically isolate the bridge from the ground plane. The oxide is SiO_2 and was deposited by sputtering. The recipe is given in Table 5.

Table 5: Recipe for silicon dioxide sputtering.

Base pressure	6×10^{-6} mTorr
Sputter pressure	1.4×10^{-2} mTorr
Argon flow	37.5 sccm
Oxygen flow	50 sccm
RF power	Forward: 320 W Reverse: 20 W
Time	70 min
Thickness	500 nm

The next step is lithography. The designed mask for the oxide layer is shown in Figure 49. The only area of the oxide layer that needs to be etched is a square on top of

the pad that will be connected to the ground of the DC power supply. Thus, the mask has only a square opening at the edge. The same recipe given in Table 3 is used for the lithography of the oxide layer. A CF_4/O_2 plasma etch was used to etch the patterned SiO_2, creating an opening over the contact pad. The recipe is given in Table 6.
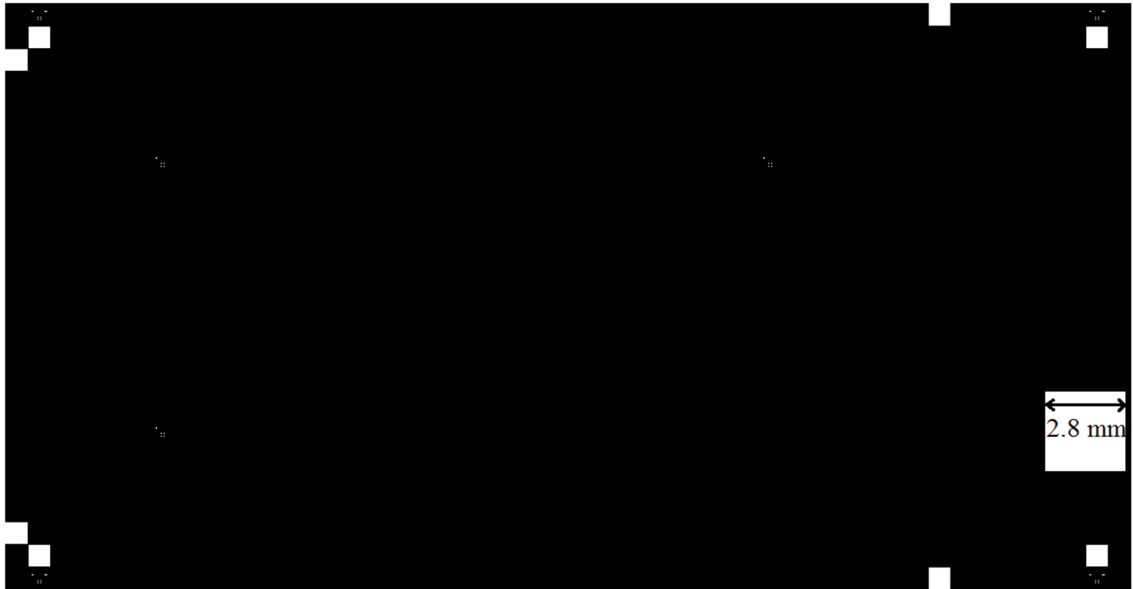
Figure 49: Designed mask for the oxide layer.

Table 6: Recipe for silicon dioxide plasma etching.

Pressure	90 mTorr
CF_4 flow	45 sccm
O_2 flow	5 sccm
ICP power	300 W
RIE power	25 W
Time	20 min
Thickness	500 nm

The plasma will not attack the underlying aluminum layer, which thus acts as a stop layer for SiO_2 etching. After etching the oxide layer, the photoresist is removed using acetone. The schematic of the fabricated device up to the second layer is shown in Figure 50.

62
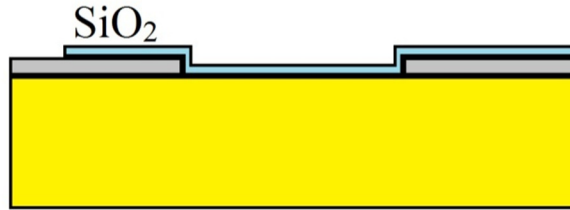
Figure 50: Deposit and patter the oxide layer.

4.3. Sacrificial Layer

A MEMS bridge is a suspended structure, therefore a sacrificial layer is needed to fabricate it. Silicon is used as the sacrificial layer. Photoresist was also tried but there are two problems with photoresist:

1. Aluminum does not adhere well to photoresist.

2. Photoresist is deposited in liquid state and has to be completely baked (and dried) to be used as a sacrificial layer, otherwise, remaining solvent inside the photoresist will bubble and the next layer on top of the sacrificial layer will come off. To vaporize all the solvent, the photoresist has to be baked for a long time, but this process caused the photoresist to crack. Further information about using photoresist as a sacrificial layer can be found in [6].

Another choice for a sacrificial layer could be copper. However, to etch copper wet etching is needed. A common difficulty when releasing suspended MEMS structures with wet etching is that the stiction force between the suspended layer and the etchant can be more than the restoring force, causing the MEMS structure to deform. For the case of the MEMS bridge, the bridge could stick to the underlying ground plane. For this reason, copper sacrificial was not selected.

63

Silicon was eventually selected as the sacrificial layer. An advantage of using silicon is the ability to use XeF_2 gas etching to remove it, which eliminates the stiction problem. It also provides a fairly isotropic etching which is essential to etch all the silicon under the aluminum layer through the holes in the bridge. The sputtering technique was used to deposit a 4 µm silicon layer. Different sputtering attempts were done to find an RF power at which the sputtered silicon had the least roughness. The RF powers; 200 W, 300 W, 400 W, and 500 W were tried. The cases of 200 W and 300 W were rougher than 400 W, and 500 W was so rough that the silicon looked black. The final recipe is given in Table 7. The schematic of the fabricated device up to the third layer is shown in Figure 51.

Table 7: Recipe for silicon sputtering.

Base pressure	6.6×10^{-6} mTorr
Sputter pressure	8.8×10^{-3} mTorr
Argon flow	64.5 sccm
RF power	Forward: 410 W Reverse: 10 W
Time	60 min
Thickness	4 µm
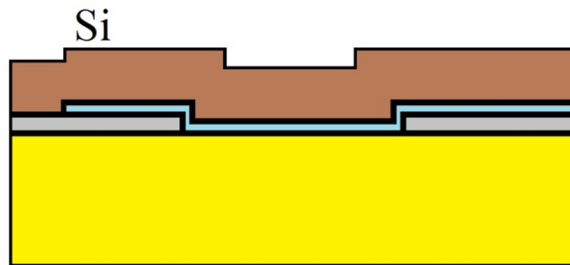
Figure 51: Deposit the sacrificial layer.

4.4. MEMS Bridge Layer

The MEMS bridge is made of aluminum, therefore, another aluminum layer is needed on top of the sacrificial layer. The criteria to choose the thickness of this aluminum layer (1 µm) were discussed in Chapter 3. The next step is lithography. The designed mask is shown in Figure 52 and Figure 53. The bias line and the pad at its end are to apply the actuation voltage to the MEMS bridge. Figure 54 shows how the ground layer and MEMS bridge layer overlap with each other. The ground layer is shown with a lighter color.
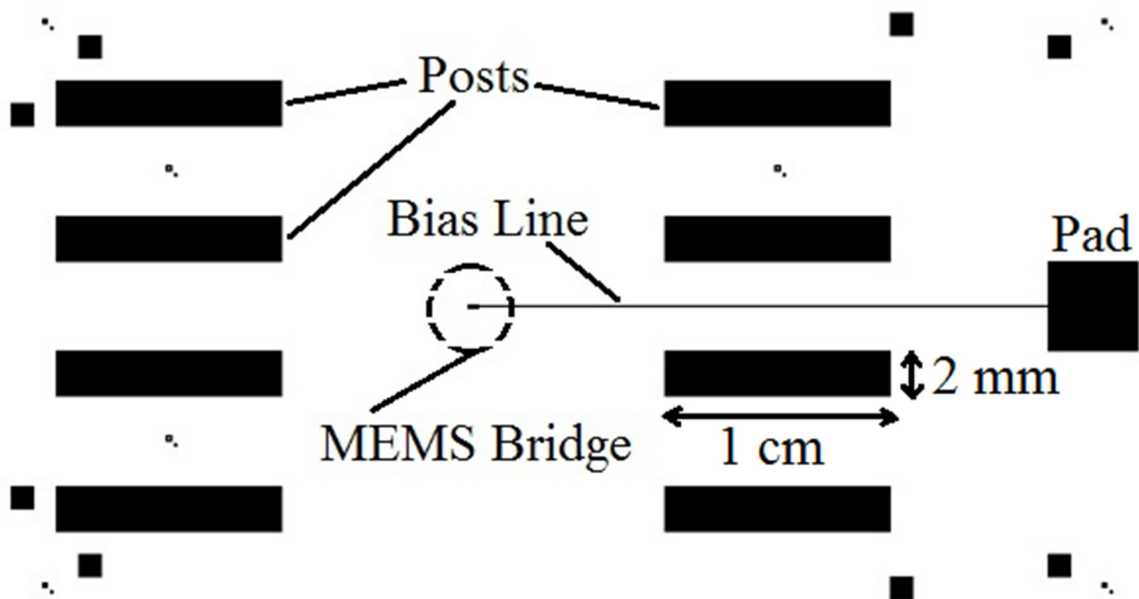
Figure 52: Designed mask for the second metal layer.
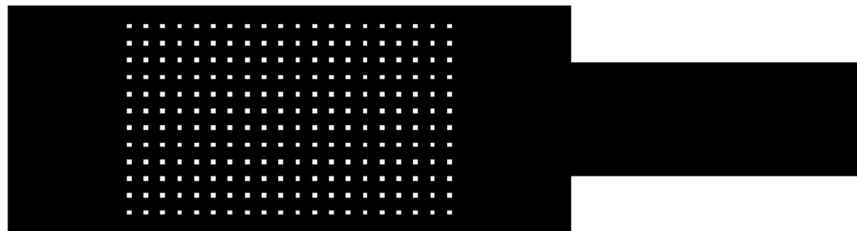
Figure 53: MEMS bridge in the designed mask for the second metal layer.
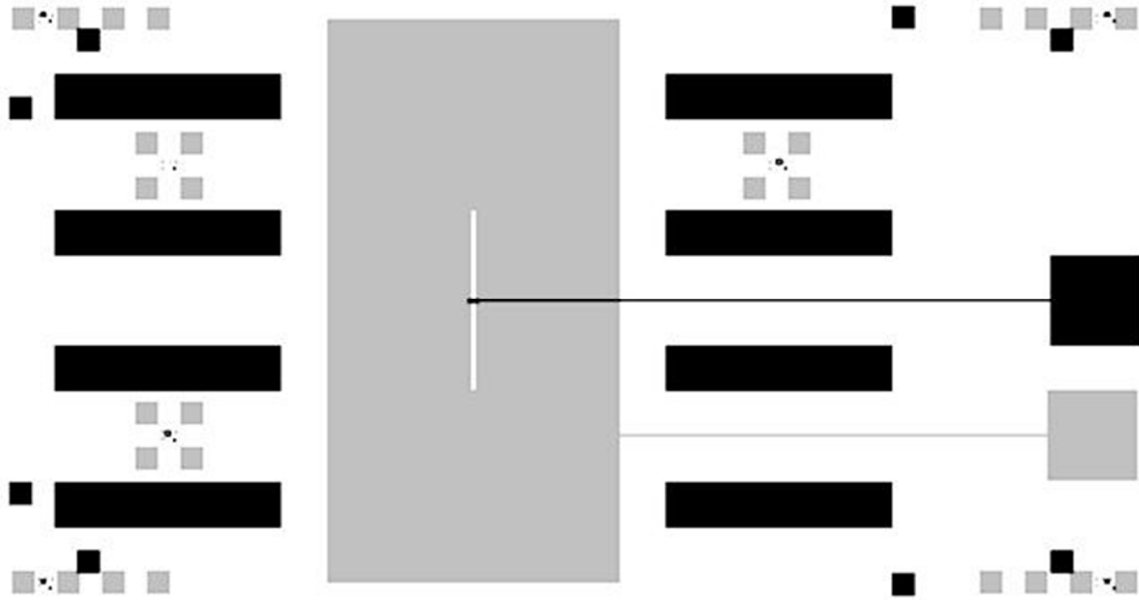
Figure 54: The two ground layer and MEMS bridge layer on top of each other.

The recipe to etch the aluminum layer is the same as Table 4. After etching the aluminum layer, the photoresist is removed using acetone. The schematic of the fabricated device up to the third layer is shown in Figure 55.
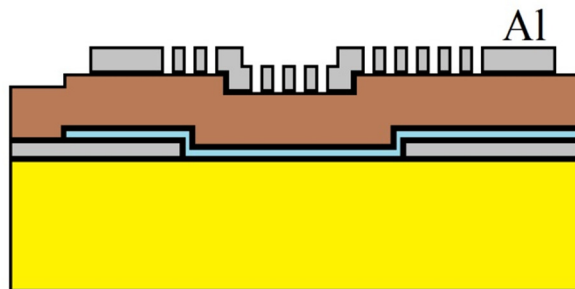
Figure 55: Deposit and pattern the second aluminum layer.

4.4.1. Issues in Patterning the MEMS Bridge

It was found that when there are many small holes in the photoresist mask, the developer does not etch the photoresist completely, and a very thin layer remains,

preventing the aluminum etch in the next step. Figure 56 shows the resulting photoresist pattern when the recipe of Table 3 was used.
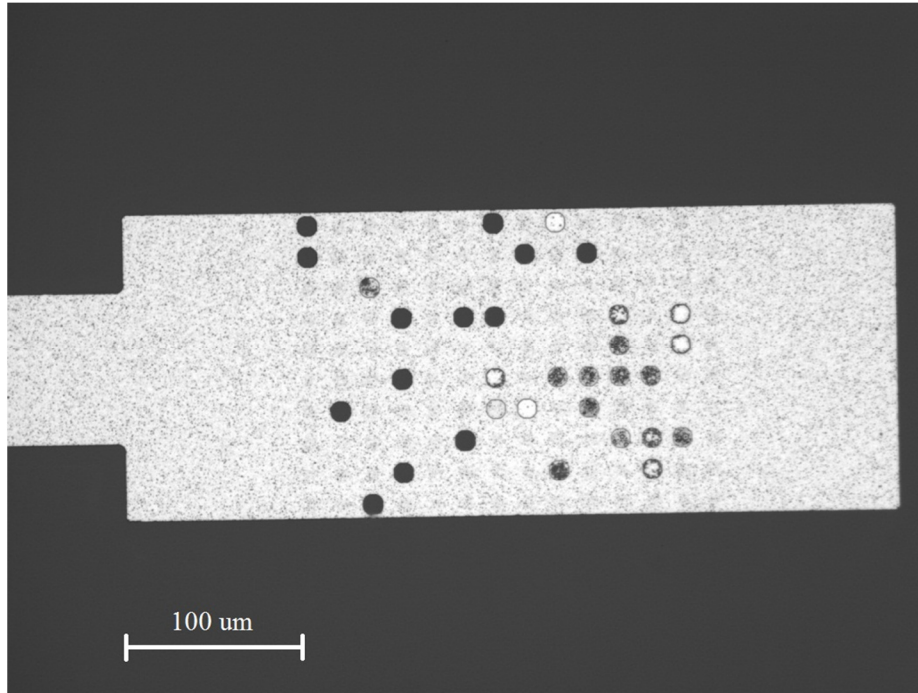
Figure 56: Holes after 4 seconds exposure and 20 seconds developing.

Different attempts were made to solve this problem by optimizing different parameters such as exposure time, developing time, baking time, and aluminum etch time. This process took about six months to develop the best lithography process.

One solution tried was to increase the exposure time. The problem with increasing the exposure time is over-exposure. Figure 57 shows a trial with the exposure time 7 seconds and developing time 20 seconds. Various other exposure times were tried, but all were unsuccessful.
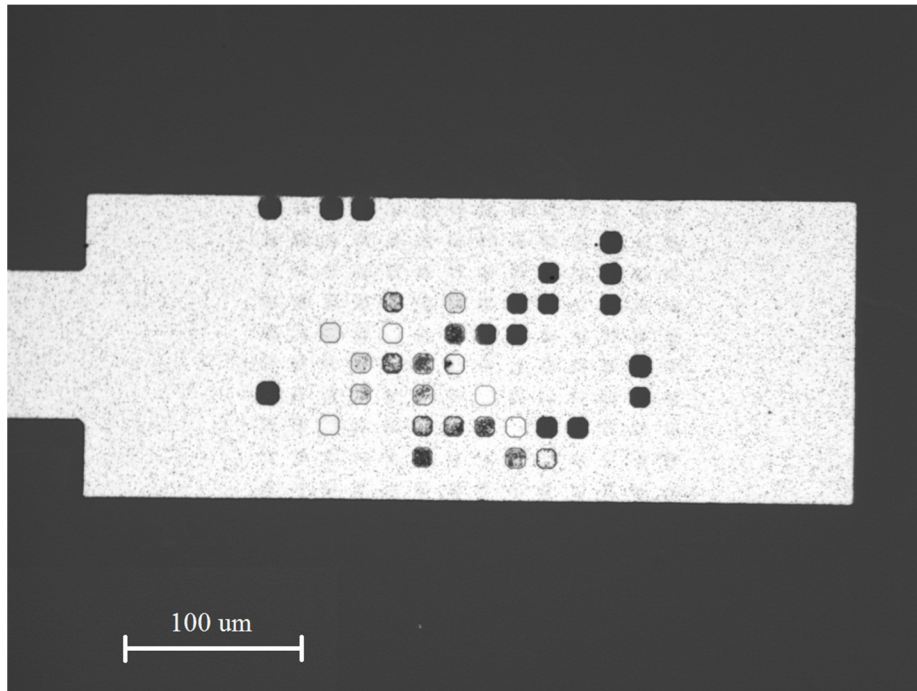
Figure 57: Holes after 7 seconds exposure and 20 seconds developing.

Another idea that was examined, was to decrease the developing time while increasing the exposure time. Although decreasing developing time can compensate for over-exposure, from experience it was found that to remove the photoresist properly a minimum developing time is required. Figure 58 shows such effect, where the exposure time remains 7 seconds but the developing time is only 10 seconds.
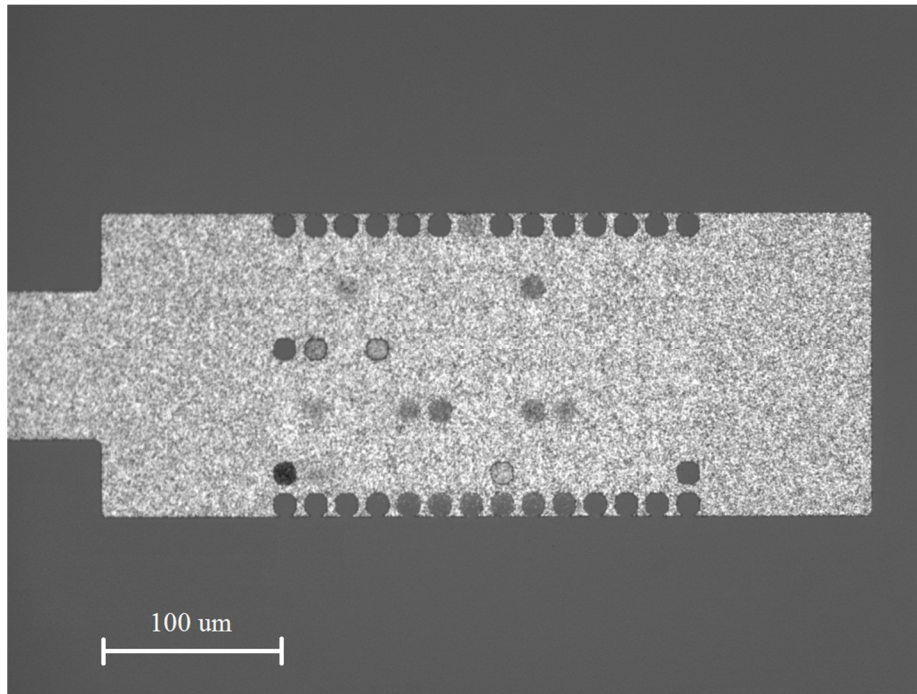
Figure 58: Holes after 7 seconds exposure and 10 seconds developing.

Increasing only the developing time does not help much. It was found that after reaching a proper developing time, increasing it more does not remove the thin layer of photoresist that remained. The final conclusion of these experiments was that any deviation from the optimized recipe in Table 3 results in bigger holes than desired. The final solution was to run a short CF_4/O_2 plasma etching after developing. This etches photoresist everywhere, and was timed long enough to remove the thin layer that remained in the holes. The recipe for the plasma etching is given in Table 8. Figure 59 shows the MEMS bridge after running the plasma etch.

Table 8: Recipe for removing the photoresist.

Pressure	200 mTorr
O_2 flow	50 sccm
ICP power	300 W
RIE power	25 W
Time	90 sec
Photoresist etched	160 nm
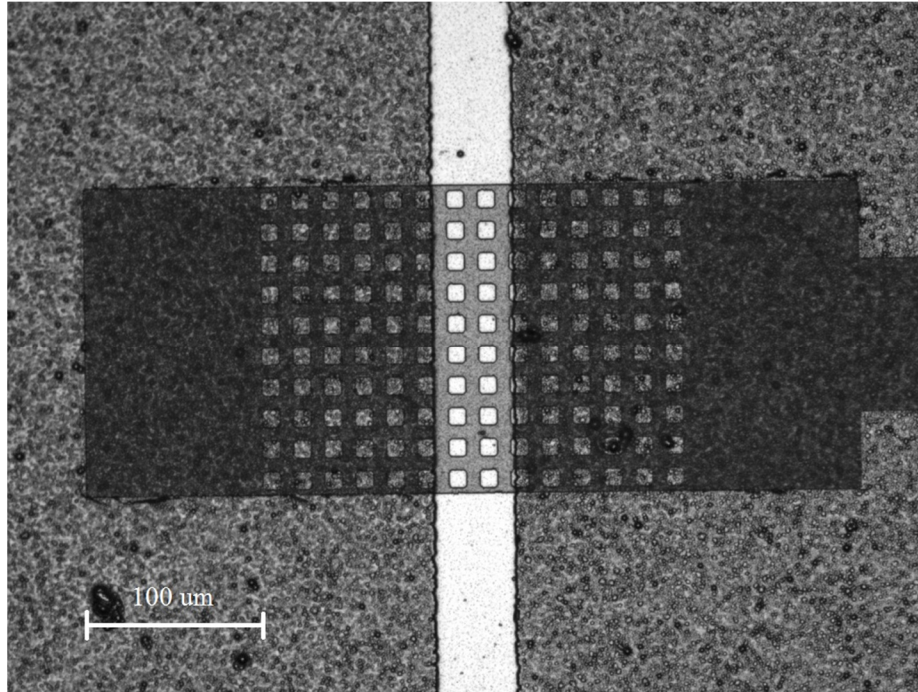
Figure 59: Holes after 4 seconds exposure, 20 seconds developing, and plasma etching of photoresist.

4.5.   Releasing the MEMS Bridge

The final step is to release the bridge by etching the silicon underneath the bridge. Different etching techniques were attempted to etch the silicon sacrificial layer and release the MEMS bridge. In the beginning, all the etching techniques failed. SF_6 plasma etch, CF_4 plasma etch, and XeF_2 etch were tried. SF_6 could not etch the silicon sacrificial layer at all. For CF_4 and XeF_2, the silicon sacrificial layer would be etched, however, a residue would be left. The residue for XeF_2 was a liquid in vacuum which would turn to a white crystalline solid after exposing to air. It took six months until I realized the frame that is used in sputtering system to hold the silicon target to the RF magnets was eroded. The plasma in the sputtering system does not normally touch the frame. More

investigations showed that one of the magnets was misaligned bending the plasma towards the frame. Therefore, the sputtered material was an alloy of silicon and the frame material which was aluminum. It was the reason that different silicon etching techniques could not remove the sacrificial layer completely. Finally, the misaligned magnet was fixed and XeF_2 etching method was used to etch the sacrificial layer since it is faster than other methods.

The difficulty with releasing the MEMS bridge is that the top aluminum layer is not transparent so it is not possible to see when the MEMS bridge is released. The solution was to develop the process using a transparent photoresist layer and measuring the number of cycles needed to etch the silicon. The image of the released photoresist is shown in Figure 60. The final recipe is given in Table 9. The schematic of the fabricated device and the actual fabricated device are shown in Figure 61 and Figure 62. Further information about using XeF_2 to etch silicon can be found in [24], [25].
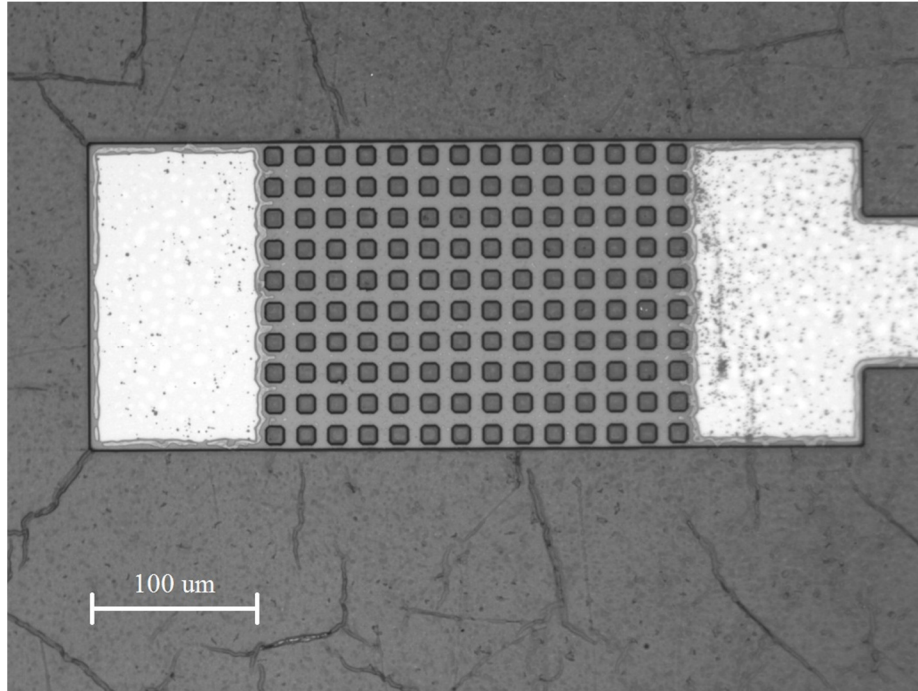
Figure 60: Etched silicon sacrificial layer under the photoresist top layer.

Table 9: Recipe for XeF$_2$ gas etching.

Number of cycles	10
Length of etching cycles	30 sec
Length of depletion cycles	30 sec
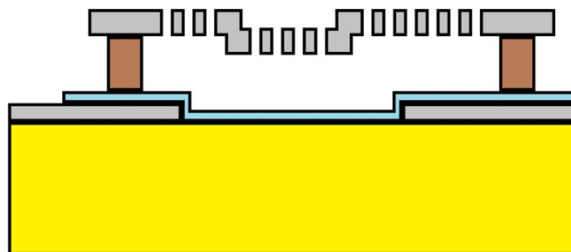
Figure 61: Etch the sacrificial layer.
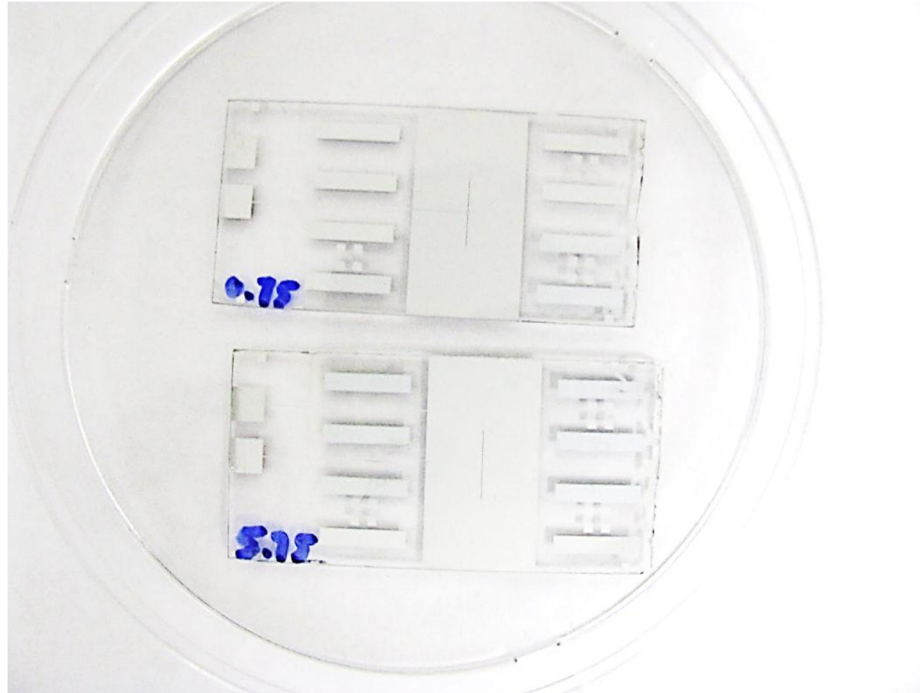
Figure 62: Final Devices.

4.6.   Unit Cell Test Assembly

The final device will be place between two X-band waveguide flanges. Figure 63 shows a fabricated device beside an X-band waveguide flange. To prevent the flange from shorting the two bias lines, two trenches with a depth of 1 mm were carved into the flange that faces the front of the device (Figure 64). The trenches prevent the flange from touching the bias lines (Figure 65). The eight posts designed in the MEMS bridge mask ensure that the flange will never make a contact with the bias lines.
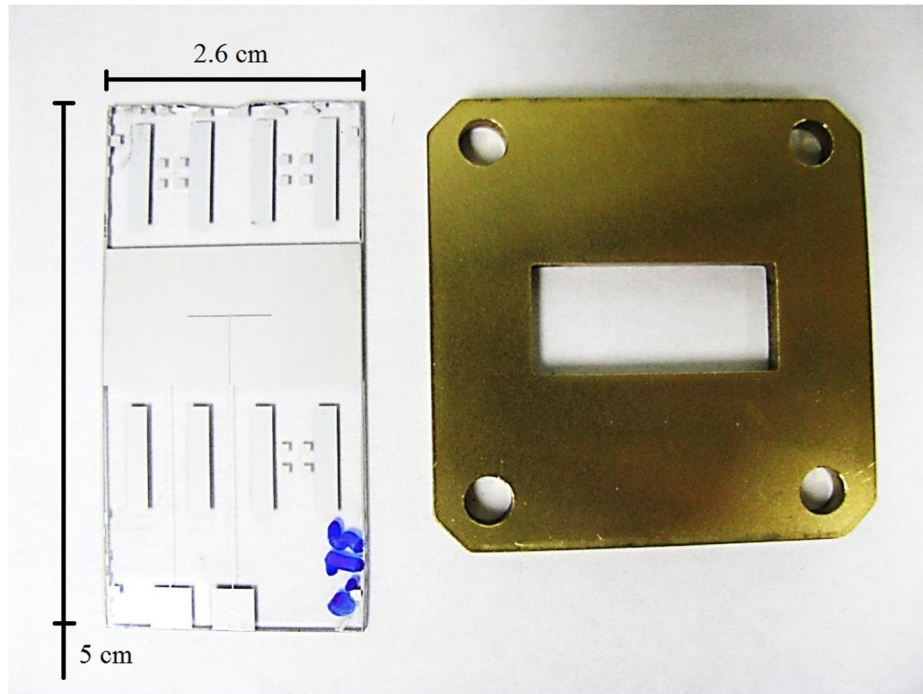
Figure 63: Fabricated device beside an X-band flange.
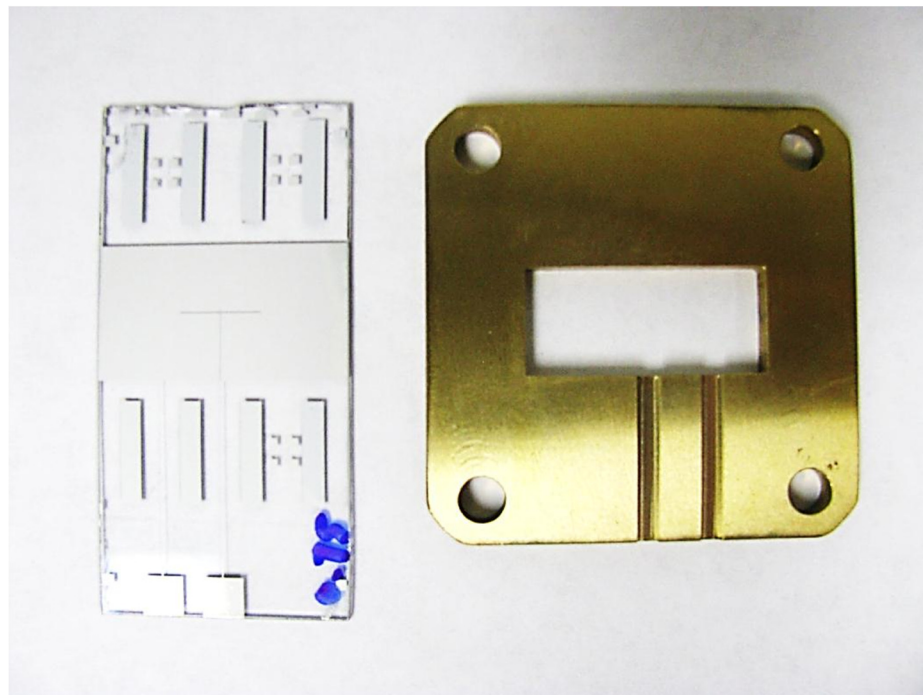
Figure 64: X-band flange with trenches.
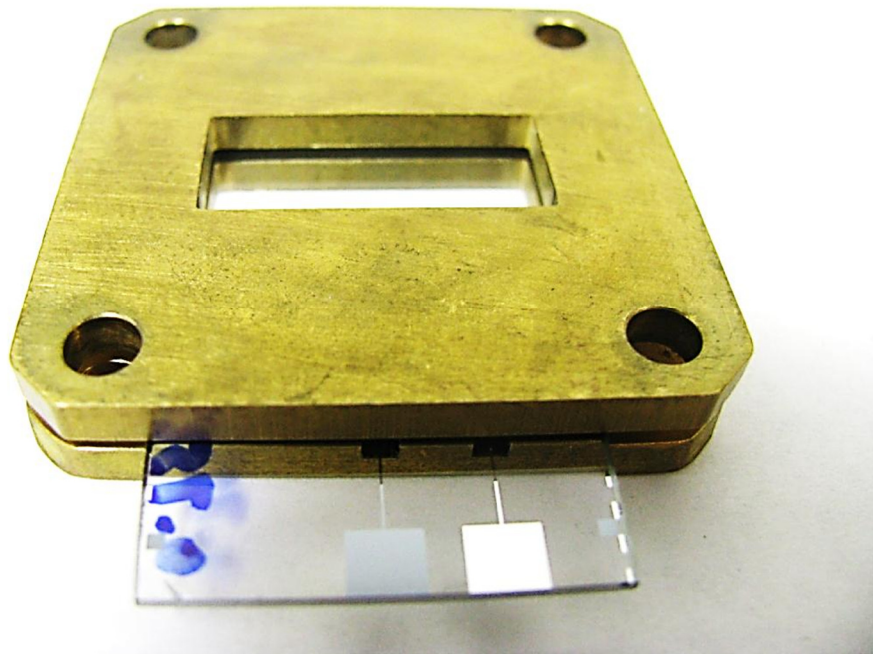
Figure 65: Fabricated device between the X-band flanges

Chapter 5

Measurements and Discussion

Similar to the approach that was used in Chapter 3 for simulation, two different tests should be done to prove the correctness of the design; mechanical measurement, and EM measurement. Mechanical measurement is discussed first to ensure that the MEMS bridge is functional and can be used to do the EM analysis. It will be explained that although the MEMS bridge could move by the applied voltage, the movement was not proper and reliable. Therefore, two samples with two MEMS bridge in two fixed up and down positions were fabricated to bypass the mechanical problem of the FSS. At the end of this chapter, a more reliable design of a MEMS bridge is shown. The design is supported by simulation results from COMSOL Multiphysics.

5.1. Electro-Mechanical Measurements

The MEMS bridge was tested to demonstrate its ability to move down by the applied voltage. This was done using a DC power supply connected to the pads at the edge of the FSS (Figure 66). The voltage was increased slowly until the MEMS bridge started to move. It was observed that at first the MEMS bridge needed about 80 V to start the movement and once it moved the actuation voltage decreased to about 60 V for the next attempts. This observation has also been seen for other MEMS devices. Using an optical microscope, the movement was observed, however, measuring the exact amount of deflection was not possible. The reasons were:

1. The voltage could not be applied for a long time since after about a minute the bias line at the edge of the ground plane will burn out. The reason could be the low quality of the sputtered silicon dioxide and its poor coverage at the edge of the ground plane. Thicker oxide layers were sputtered to try to solve this problem, however, the thicker the oxide was, the higher actuation voltage was needed, which again causes burning the bias line at the edge of the ground plane. Therefore, increasing the thickness of the oxide layer is not a proper solution. A good solution is using another deposition technique such as thermal oxidation of silicon to improve the quality of the insulator.

2. Another difficulty with the measuring the deflection of the MEMS bridge was that the MEMS bridge would warm up due to leakage of the electrical current between the MEMS bridge and the ground plane and change its shape. This occurs because of the poor quality of the insulator and also the sacrificial layer that was discussed in the Section 5.1.3 Again, improving the quality of the insulator and the sacrificial layer could solve this problem.

Figure 66: MEMS bridge mechanical measurement setup.

The problems discussed above can be solved by using alternative fabrication techniques. Apart from these problems, it was noticed that the MEMS bridge is not flexible enough due to its simple rectangular shape. In fact, for a more reliable design, the anchors should be narrower than the middle of the MEMS bridge because most of the bending of the MEMS bridge occurs at its anchors. A more profound discussion on this matter is in Section 5.3.

5.2. EM Measurements

The final goal of this thesis is to demonstrate that the resonance frequency of the designed FSS can be changed. Generally speaking, there are two types of methods to measure the scattering parameters of an FSS:

1. Fabricating a large FSS so that it can be considered as a periodic structure. Using two horn antennas at two sides of the FSS to obtain the scattering parameters. The disadvantage of this method is that it takes more effort to fabricate a large array of elements and diagnosis would be difficult. Also the radiation pattern of the horn antennas has a main lobe in the middle which does not provide a plain wave for all the elements of the FSS.

2. Fabricating only one element of the FSS and put it inside a waveguide simulator to obtain the scattering parameters. Assuming a plane vertical/horizontal polarized wave illuminates the FSS, the electric field has to be parallel to two walls of the FSS element and perpendicular to the other two walls; therefore to obtain the scattering parameters of the FSS with only one of its elements as a cell, one has to impose Perfect Electric Conductor (PEC) and Perfect Magnetic Conductor (PMC) boundary conditions to perpendicular and parallel walls, respectively. The fact that all the four walls in a waveguide are PEC causes a slight shift in the resonance frequency of the measured FSS, which is the disadvantage of using waveguide simulator. However, if one uses the same four PEC boundaries configuration in simulation, the measurement and simulation results would presumably match. The shift in resonance frequencies due to using four PEC boundaries was discussed in Section 3.5.

In this thesis, a waveguide simulator is used to do the measurements (Figure 67). Two flanges were made to prevent the waveguide from touching the bias lines. In fact one flange with two trenches in it would be enough but the two are used to maintain the

symmetry. Coaxial to waveguide adaptors are used to connect the network analyzer. An

Anritsu ME7808A network analyzer was used to do the measurements (Figure 68).
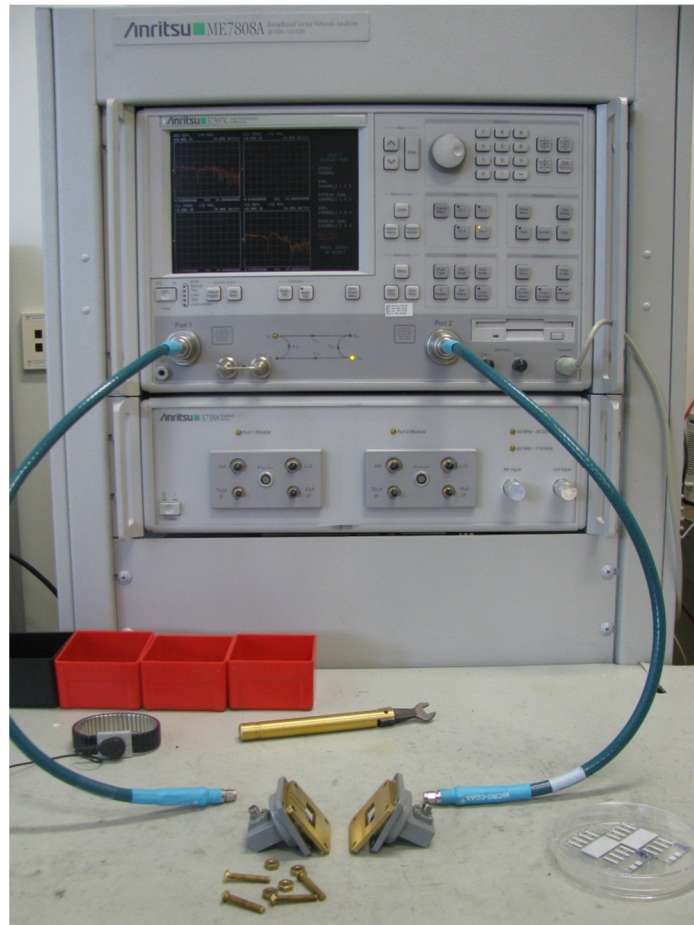
Figure 67: Scattering parameter measurement setup.
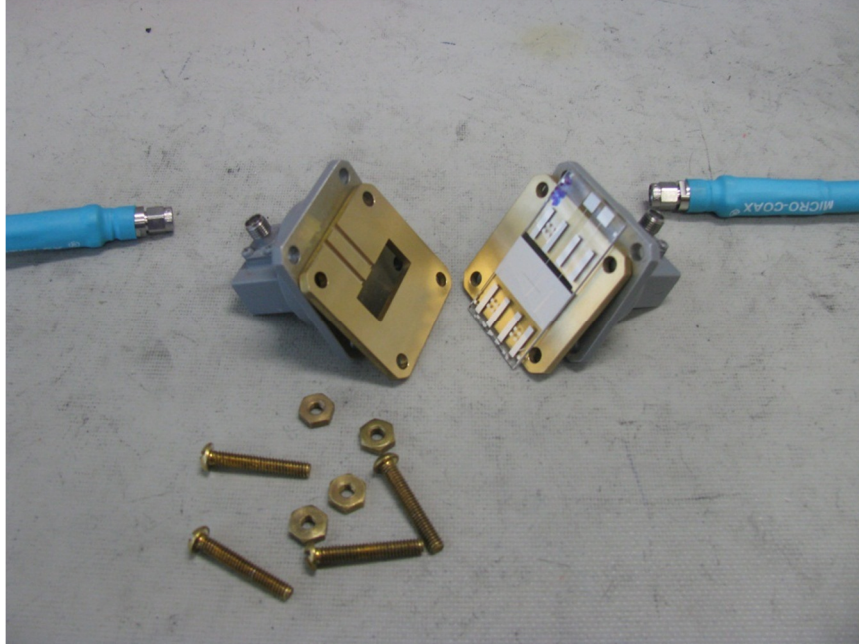
Figure 68: Waveguide simulator.

5.2.1. Measured Reflection Coefficients

From the operation principle discussed in Section 3.2, it is expected that by decreasing the height of the MEMS bridge, the equivalent capacitance of the FSS increases, which in turn decreases the resonance frequency of the FSS. This can be investigated by obtaining the reflection coefficient of the FSS by applying different actuation voltages to the MEMS bridge to change its height. However, due to the mechanical problems of the MEMS bridge discussed in Section 5.1, two different samples were fabricated with two different heights of the MEMS bridge to provide two up and down position of the MEMS bridge. This way, we can bypass the mechanical actuation of the MEMS bridge and only investigate its frequency response.

The criteria to choose the two different heights of the MEMS bridge is that they should be far enough to demonstrate a noticeable shift in resonance frequency. Therefore,

two samples with two different heights of the MEMS bridge, 5.75 µm and 0.75 µm, were fabricated. Figure 69 shows the reflection coefficients of the two FSS. It can be seen that the resonance frequency of the FSS decreases by 1.25 GHz for the height 0.75 µm as compared to the height 5.75 µm. The results serve the idea that the resonance frequency decreases by decreasing the height of the MEMS bridge.
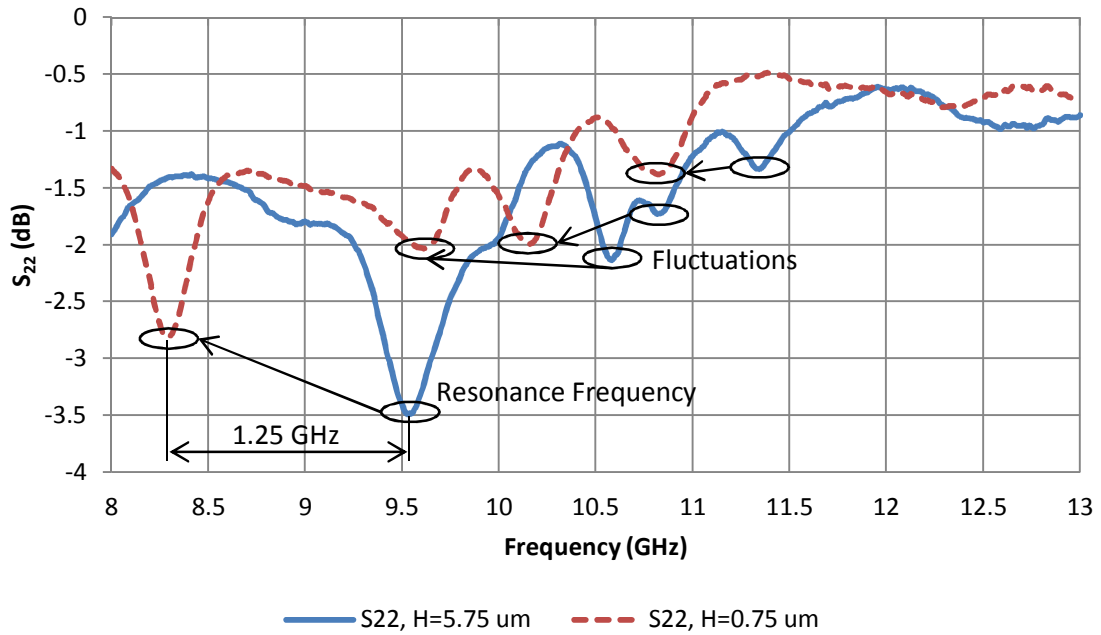
Figure 69: Measured reflection coefficient of the FSS for two different heights of the MEMS bridge.

The two chosen heights of the MEMS bridge, 0.75 µm and 5.75 µm were not presented in Figure 42. Therefore two more simulations for these heights were done to have a better comparison between the simulation and measurement results. The simulated reflection coefficients along with the measured ones are shown in Figure 70. Although both simulation and measurement show the shift in resonance frequency, it can be seen that there are two major differences between simulation and measurement results. First, the notches of the measured reflection coefficients are smaller than those of simulated

reflection coefficients. For a good reflector/transmitter the loss of the desired coefficient has to be less than -10 dB to ensure a good quality signal. This criteria is present in the simulations but not in the measurements. Second, the corresponding resonance frequency of the simulation and measurement results are off with a noticeable value. These observations lead us to two questions:

Q 1.   Why is the reflection coefficient at the simulated resonance frequencies around -23 dB, but at the measured resonance frequencies only around -3 dB?

Q 2.   Why do the measured resonance frequencies not match those of simulation?

In the next sections of this chapter, these two questions are answered and the solutions to the problems are discussed.
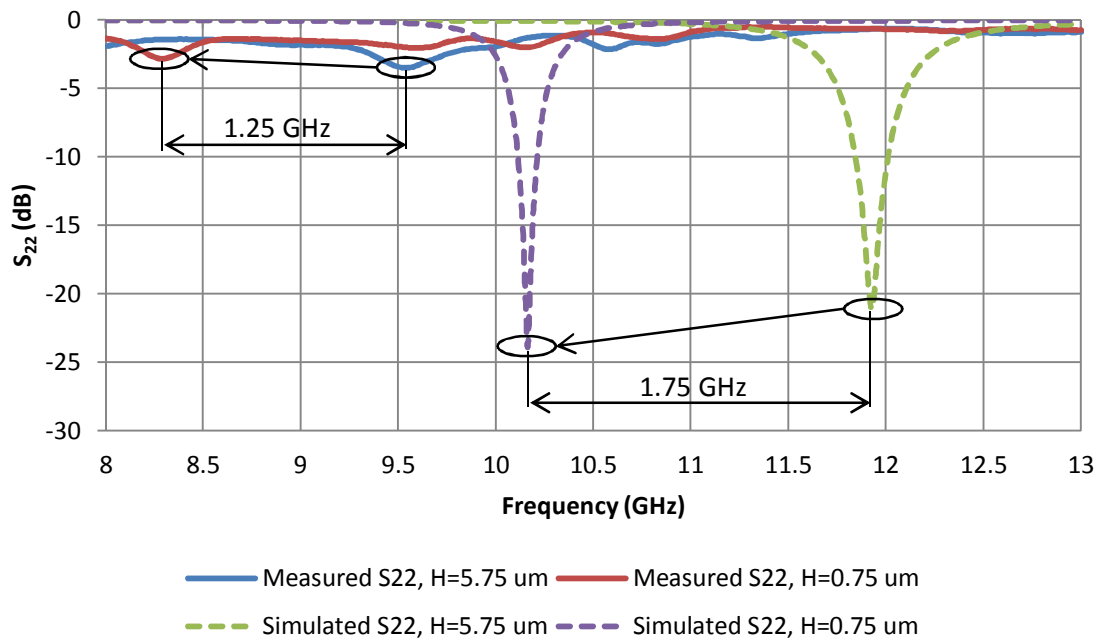
Figure 70: Measured and simulated reflection coefficients.

5.2.2. Effect of the Sacrificial Layer Conductivity

To answer Question 1, it is important that the sacrificial layer be a good insulator; otherwise it degrades the frequency response of the FSS. A simulation was done for a 4 µm thick sacrificial layer with different conductivities to see the effect of sacrificial conductivity on reflection coefficient. The results are shown in Figure 71. It can be seen that the conductivity of the sacrificial layer should be less than about 0.1 S/m, for the reflection coefficient at the resonance frequency to be better than -10 dB. This suggests that for conductivities of the sacrificial layer more than 0.1 S/m, the loss at the resonance frequency is worse than -10 dB.
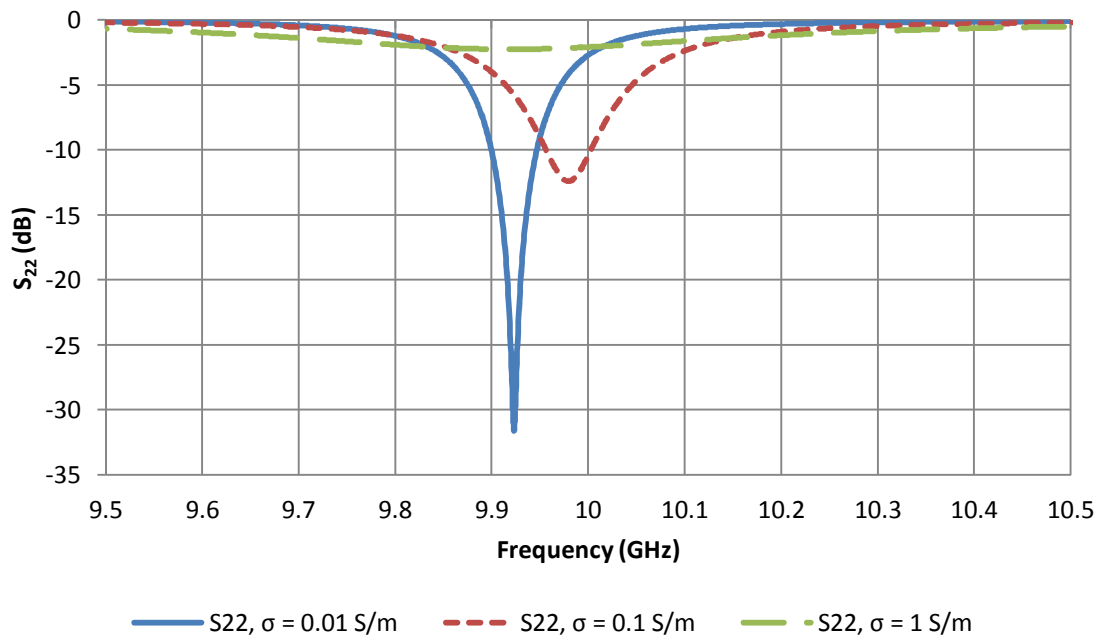
Figure 71: Simulated reflection coefficient of the FSS for three different conductivities of the sacrificial layer with the thickness 4 µm.

The conductivity of intrinsic silicon is in the order of 10^{-3} S/m, but if it has even a small amount of impurities, its conductivity increases drastically. According to the

discussion above regarding Figure 71, the conductivity of the sputtered silicon layer is higher than intrinsic silicon, which has caused the degradation of the reflected wave. The high conductivity of the sputtered silicon is possibly due to contamination since it was noticed that the clamp that is used to hold the silicon target to the frame was eroded. The erosion could be due to sputtering of the clamp along with the silicon target. The remedy to solve the high conductivity is to use a good insulator as the sacrificial layer.

A four-point probe measurement technique was used to verify that the silicon sacrificial conductivity was too high. Conductivities were measured at six different spots of the sacrificial layer, and their average was 555 S/m. This conductivity is much larger than 0.1 S/m, which explains the reason for the small reflection coefficient at the resonance frequencies. In fact, a conductive sacrificial layer leaks the current induced by the incident wave between the MEMS bridge and the ground plane and weakens the reflected wave from the FSS.

Figure 72: Four-point probe measurement device.

5.2.3. Effect of the Bias Line

The cause of the problem stated in Question 2 is neglecting the bias line in the simulation (Figure 31). A new structure with a bias line and a 5.75 µm thick silicon sacrificial layer was simulated (Figure 73). The final fabricated device is also shown in Figure 74 to show the actual bias line passing over the ground plane. Figure 75 shows the reflection coefficients before and after including the bias line in the structure. The reason for the decrease in the resonance frequency after including the bias line is that the bias line adds to the capacitance of the FSS, hence decreases the resonance frequency.
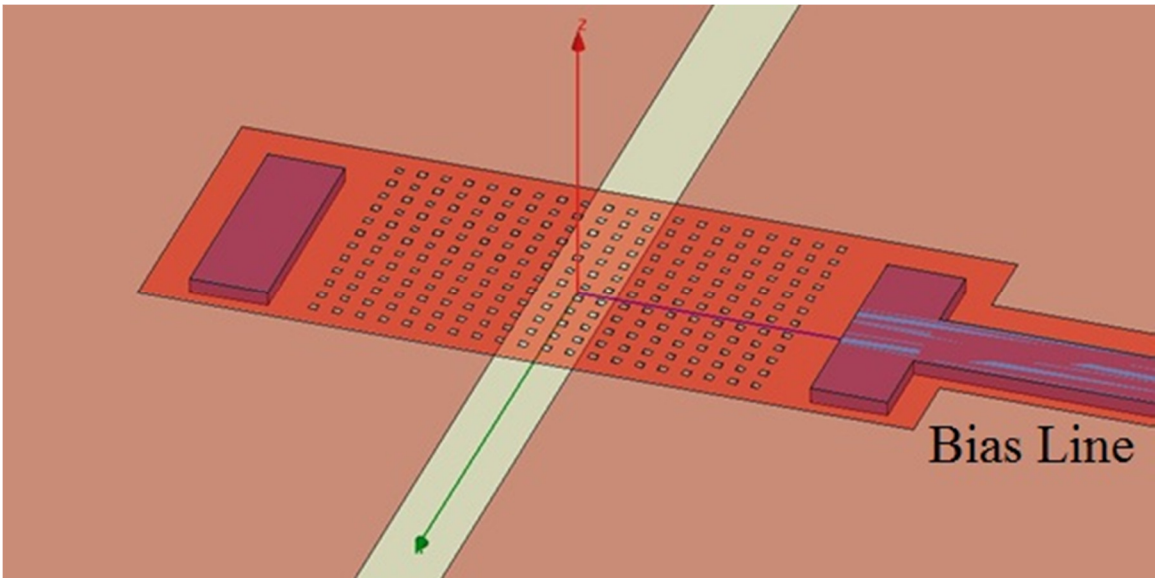
86

Figure 73: MEMS bridge with bias line.
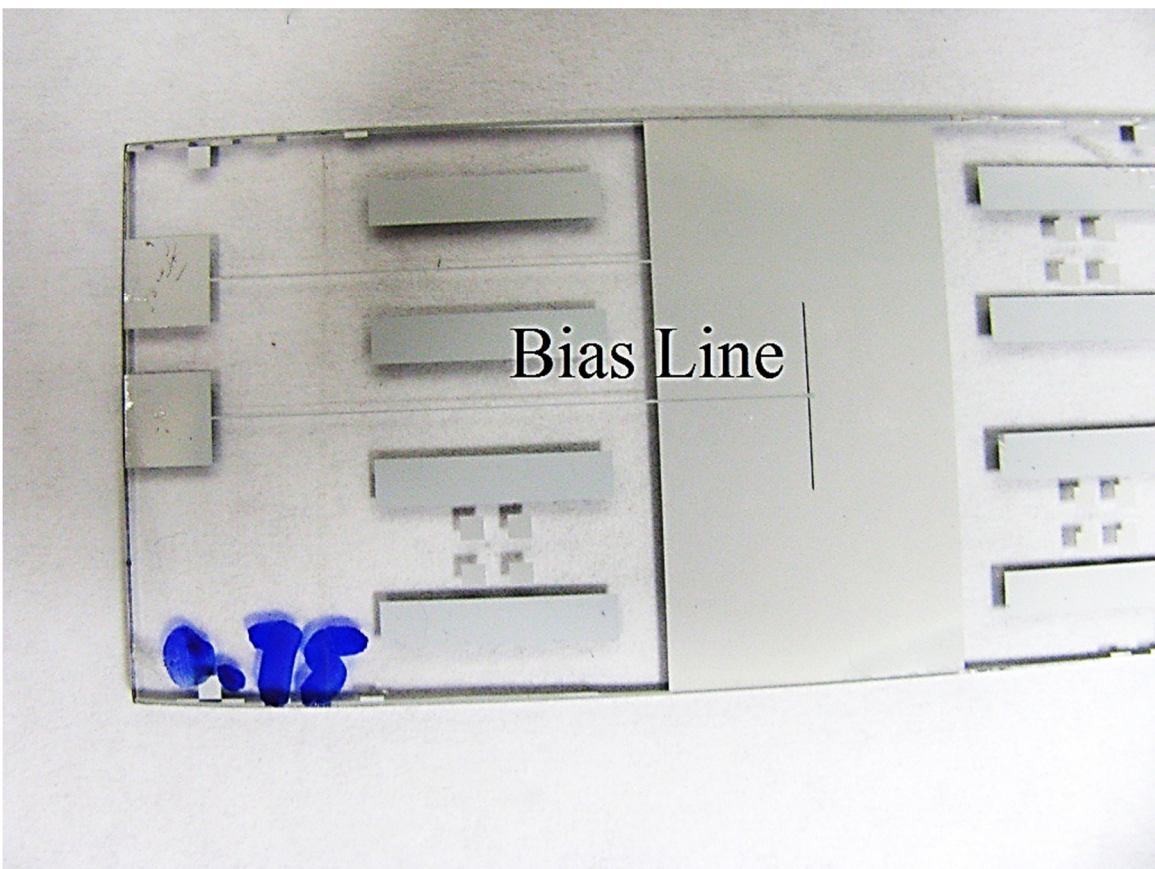
Figure 74: Fabricated device with bias line.

87
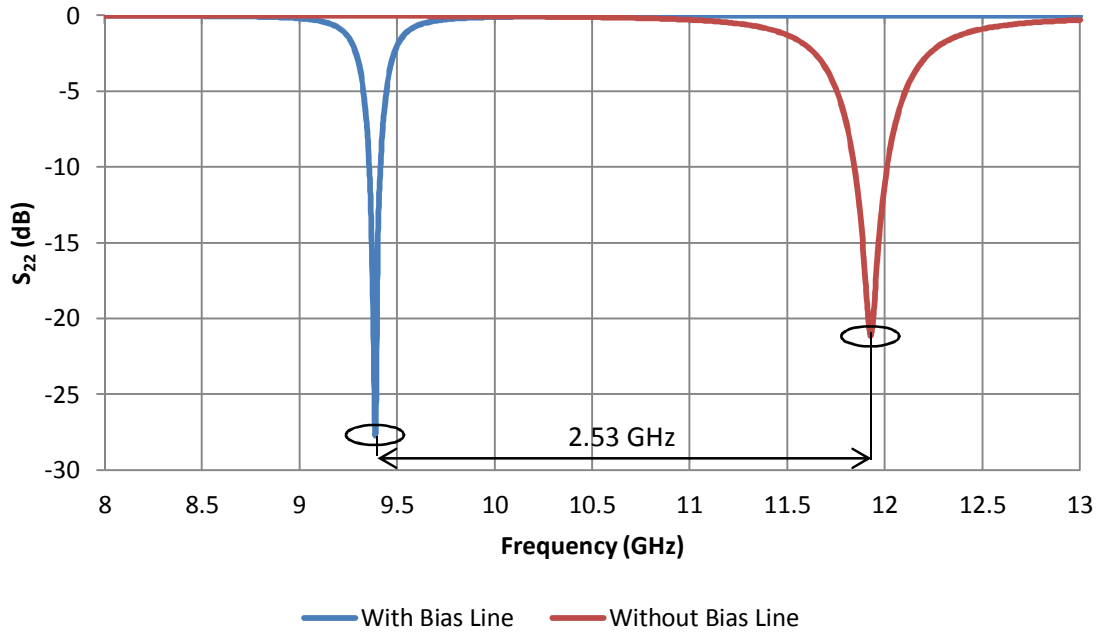
Figure 75: Simulated reflection coefficients for the height of the MEMS bridge 5.75 µm with and without the bias line (the height of the bias line is also 5.75 µm).

According to Figure 69, the resonance frequency of the fabricated device with the height of the MEMS bridge equal to 5.75 µm is 9.53 GHz. It can also be seen in Figure 75 that the resonance frequency of the simulated device after including the bias line is 9.39 GHz, proving that after including the bias line in the simulation, the measured and simulated results are in good agreement.

Another set of simulations were done for different widths of the bias line and the reflection coefficients are shown in Figure 76. It can be observed that the resonance frequency increases as the width of the bias line decreases. The reason is that by decreasing the width of the bias line, its surface area decreases, which in turn decreases the capacitive load caused by the bias line. Therefore, the resonance frequency increases. It can be seen in Figure 76 that the resonance frequency of the FSS with the width 4 µm occurs at 10.76 GHz, which is still much lower than the resonance frequency for the

simulated FSS without bias line in Figure 75 (11.93 GHz). Practically, it is not possible to choose widths of the bias line less than 40 µm since in the fabrication process when the MEMS bridge is released, the sacrificial layer underneath the bias line will be completely etched and the bias line will come off. It would be ideal if it were possible to choose a narrow bias line, such as 2 µm, which would perhaps eliminate the effect of the bias line. However due to the fabrication limitation, it is not possible. Therefore, the shift in the resonance frequency of FSS has to be included in the simulation before designing the structure so that the simulated and measured results match.
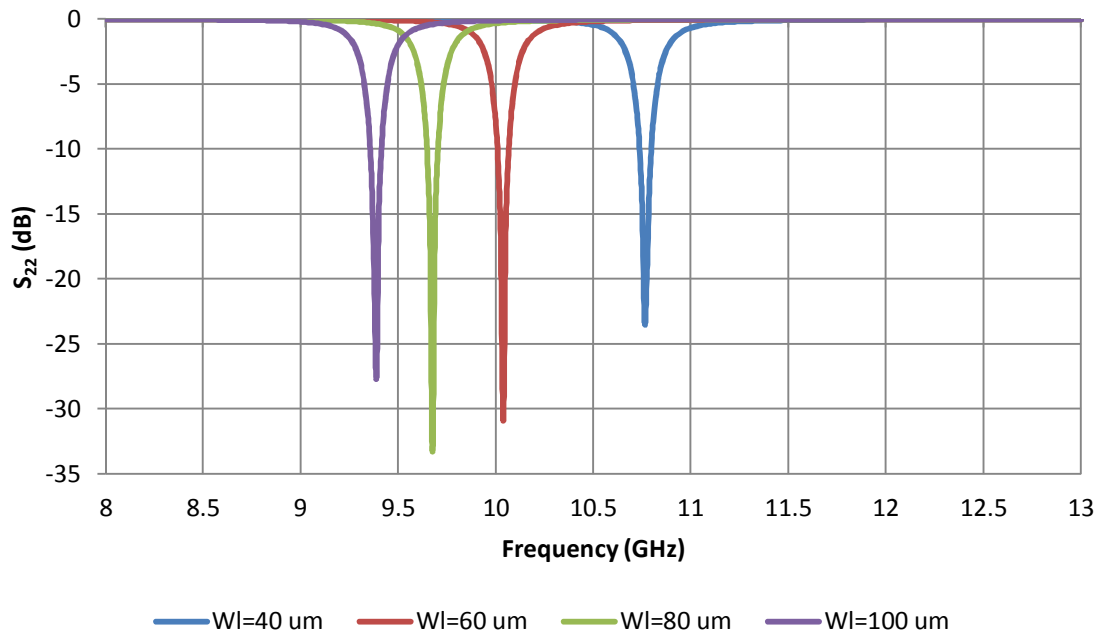
Figure 76: Simulated reflection coefficients for different widths of the bias line (the height of the bridge and bias line is 5.75 µm).

It is noteworthy to emphasize that all the reflection coefficient plots in this thesis are either for the case where there is no bias line or the bias line has the same height as the MEMS bridge. A careful reader might ask what happens when the bias line is fixed at some height and only the MEMS bridge bends down? Is the MEMS bridge still able to

provide a significant resonance frequency shift? To answer this question, another simulation was done to investigate the reflection coefficient of the FSS for different heights of the MEMS bridge, when the bias line is fixed at the height of 5.75 µm. The results are shown in Figure 77. It can be seen that the MEMS bridge is still able to provide a comparable capacitance to the capacitance of the bias line and shift the resonance frequency from 9.39 GHz for the height of 5.75 µm to 8.14 GHz for the height of 1 µm. It is also important to notice that as it can be seen in Figure 42, the majority of the shift in the resonance frequency of the FSS happens after the height of 1 µm. Unfortunately for the Figure 77, this is not possible since the resonance frequency for the height of 1 µm is already at the beginning of the X-band frequency range. This again shows the drawback of not considering the bias line in the design of the FSS.
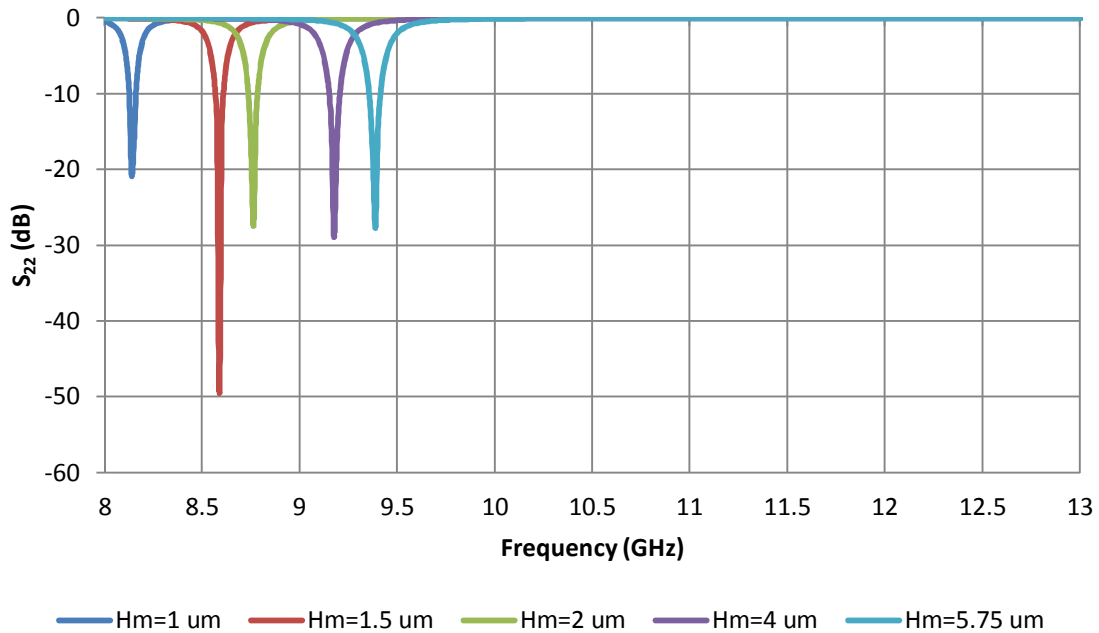

Figure 77: Simulated reflection coefficients for different heights of the MEMS bridge (the height of the bias line is 5.75 µm).

5.3. New Design

In the previous sections, the electro-mechanical and EM measurement results were shown and it was explained that the proposed FSS has some problems in its both mechanical and EM operations. The solutions were also discussed. In this section, a new design for the FSS is presented.

5.3.1. Improving the Movement of the MEMS Bridge

It was discussed in Section 5.1 that due to the uniform rectangular shape of the MEMS bridge in Figure 31, it becomes stiff at its anchors where much of the deflection occurs, therefore, decreases the flexibility of the MEMS bridge. To solve this problem, one can make the MEMS bridge narrower at its anchors. However, making the MEMS bridge narrow at its two ends causes twisting while deflecting. To solve the twisting problem, the MEMS bridge can have two anchors at each side. An even more flexible design is using spring arms to connect the membrane to the posts. The design is shown in Figure 78. The structure is cut in half and a symmetry plane is assigned to the boundary of the two halves to simplify the simulation.
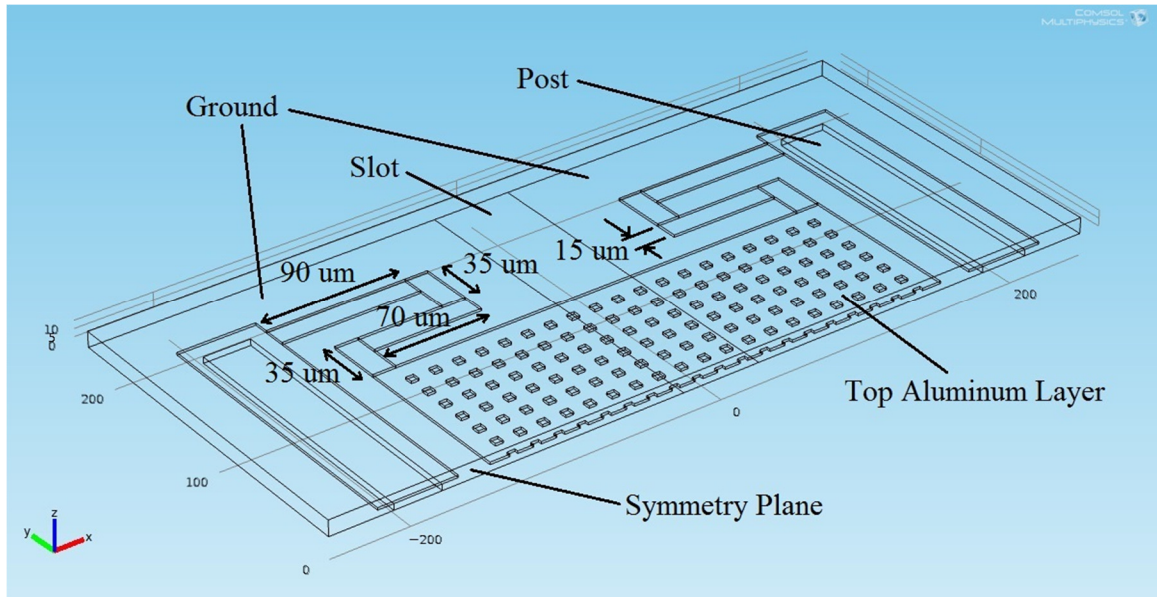
Figure 78: New MEMS bridge.

To show that the MEMS bridge deflects by the actuation voltage V_{in}, a color plot of the deflected MEMS bridge at the applied voltage 13.5 is shown in Figure 79. It can be seen that most of the deflection happens at the first arm of the MEMS bridge. This makes the movement of the MEMS bridge almost planar, which makes the EM simulation more accurate than the case without arms. Figure 80 shows the deflection of the middle of the new MEMS bridge for different applied voltages. The simulation was done using COMOSL Multiphysics. It can be seen that the snap-shut voltage has decreased to 13.5 V for the same size MEMS bridge as compared to the results plotted in Figure 40.

Figure 79: Displacement of the new MEMS bridge at the actuation voltage V_{in}=13.5 V.

Figure 80: Deflection of the new MEMS bridge at its middle vs. actuation voltage.

5.3.2. Improving the Quality of the Insulator and Sacrificial Layers

The old FSS design had the problem of leakage of DC current between the MEMS bridge and the ground, and also burning out 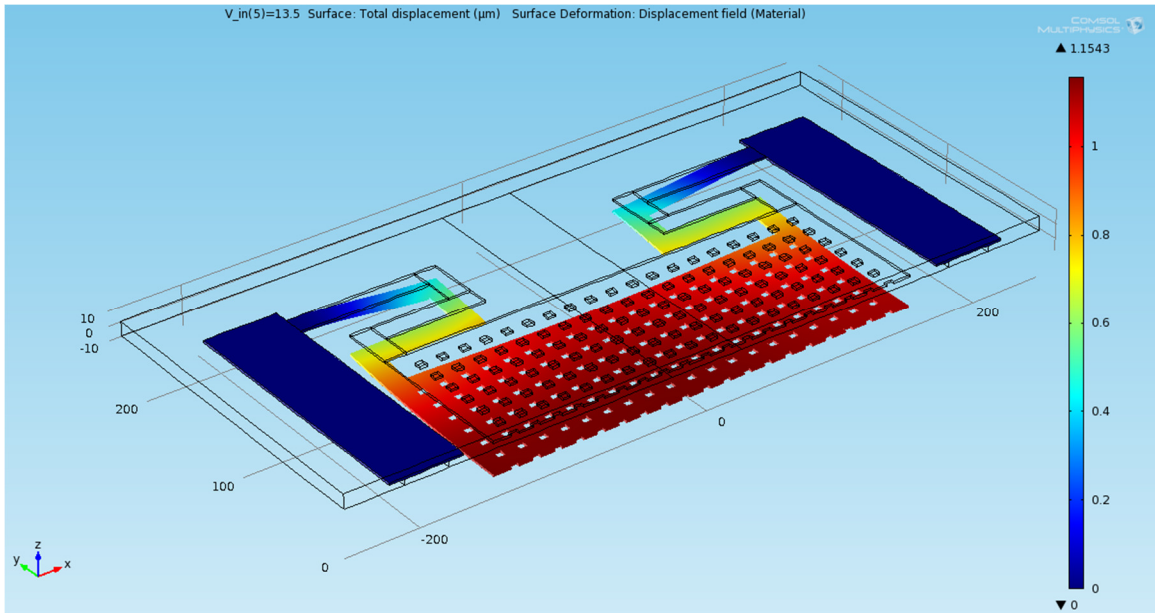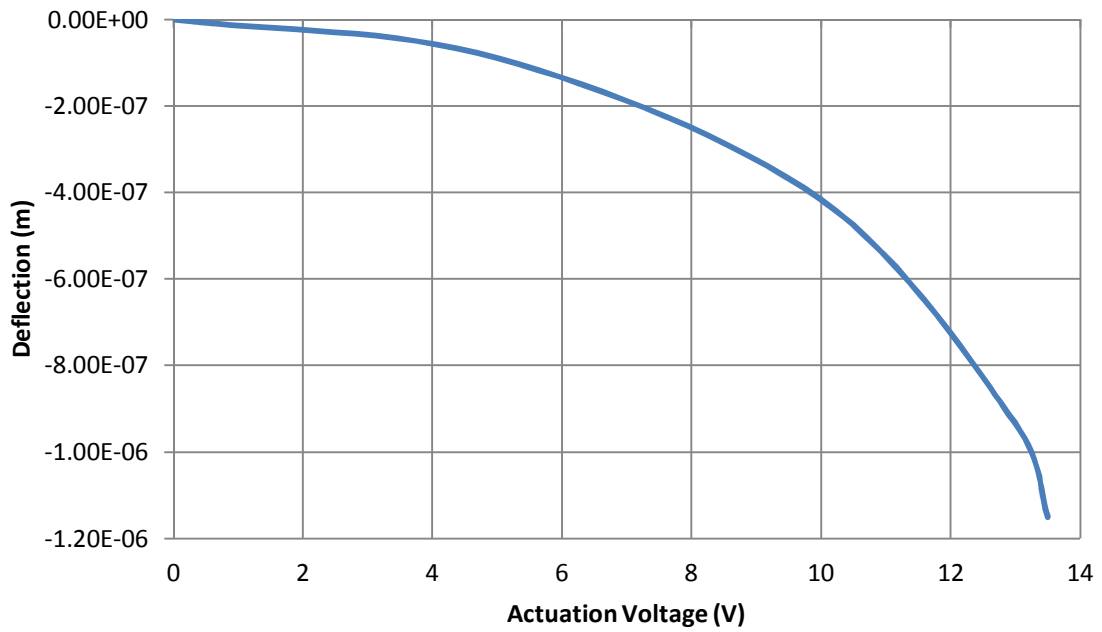of the bias line. Both of these problems are solved in the new design by using thermal oxidation to deposit a better quality SiO_2.

Another problem was the sacrificial layer and its high conductivity that degrades the reflected wave. In the new design, silicon is to be deposited by using PECVD to achieve a better quality.

5.3.3. Adjusting the Frequency Response of the FSS

Finally, the effect of the bias line has to be reduced. In the new design, the width of the bias line is decreased from 100 μm to 50 μm. Also, the length of the slot has to be adjusted to account for the effect of the bias line on the resonance frequency of the FSS. The goal is to set the resonance frequency at the end of X-band frequency range, when the MEMS bridge is in the up position. Therefore, a simulation was done using Ansoft HFSS to obtain reflection coefficients of the new FSS for different lengths of the slot while the MEMS bridge is in the up position. The sacrificial layer is intrinsic silicon. The results are shown in Figure 81. It can be seen that for the length of the slot equal to 4 mm, the resonance frequency occurs at the end of the X-band frequency range. Therefore in the new FSS, the length of the slot was chosen to be 4 mm. It is noteworthy to mention that the bandwidth of the reflection coefficient decreases by decreasing the length of the slot, which is another advantage of using a smaller slot.
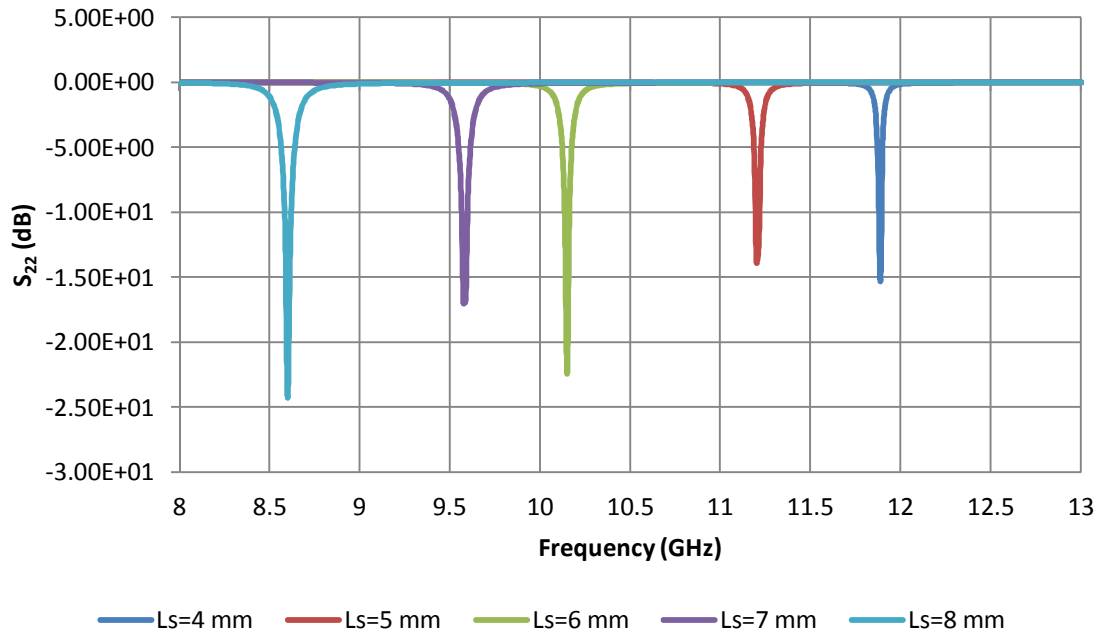
Figure 81: Simulated reflection coefficients of the new FSS for different lengths of the slot while the MEMS bridge is in the up position.

Finally, Figure 82 shows simulated reflection coefficients of the new FSS for different heights of the MEMS bridge. The sacrificial layer is intrinsic silicon. It can be seen that when the MEMS bridge is in the up position (H = 4 µm), the resonance frequency occurs at the end of X-band frequency range, and when the MEMS bridge is in the down position (H = 0.25 µm), the resonance frequency occurs at the beginning of the X-band range. The height of the bias line is 4 µm. The simulation was done using Ansoft HFSS and the design is shown in Figure 83.
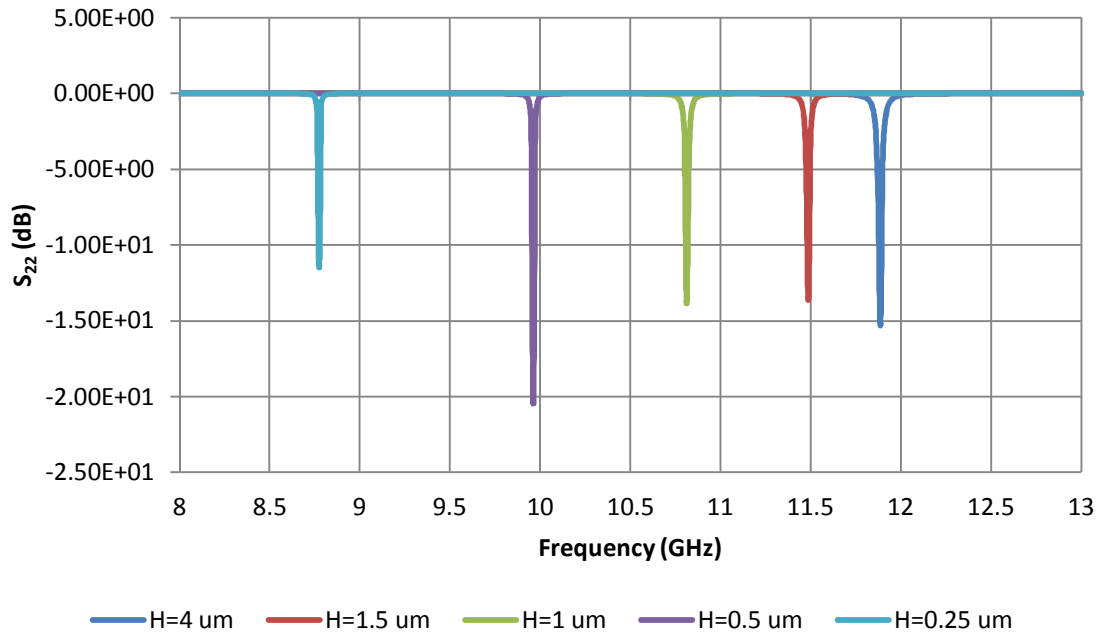
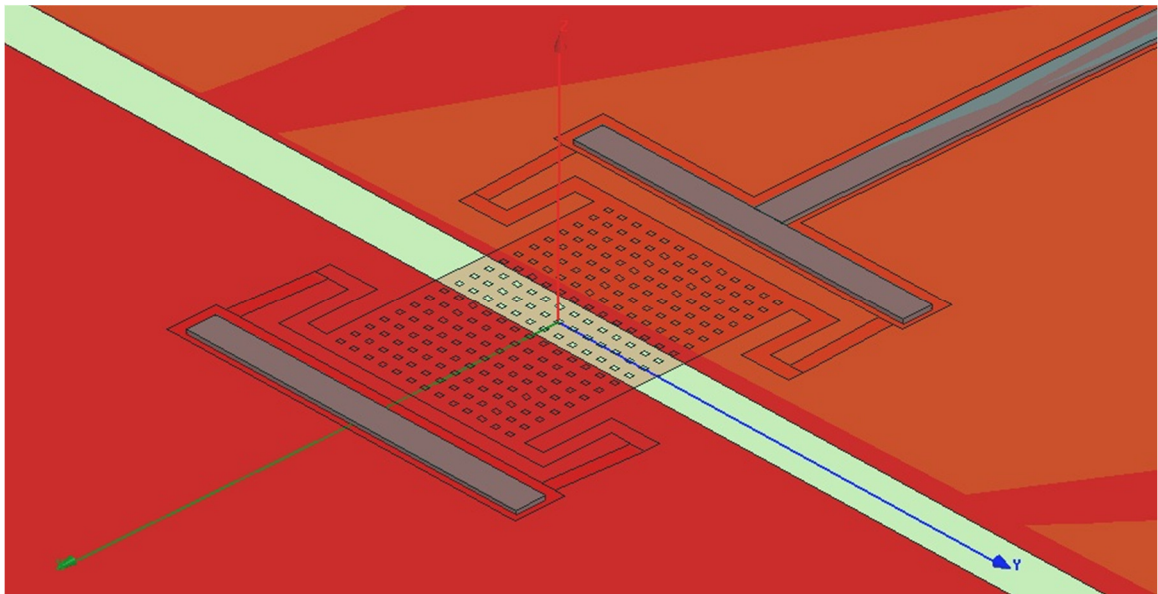Figure 82: Simulated reflection coefficients of the new FSS for different heights of the MEMS bridge.

Figure 83: New FSS design in Ansoft HFSS.

Chapter 6

Conclusions and Future Work

An innovative reconfigurable FSS design has been proposed. The advantage of the proposed design is to eliminate the need for having multiple MEMS structures, and to provide a significant shift in resonance frequency. It also uses the ground plane as the pull-down electrode and makes the fabrication process simpler.

The design procedure and important considerations have been discussed. The concept of operation together with the simulation and measurement results have been presented. The results prove the correctness of the theory that has been offered to describe the operation principle of the FSS.

Different methods of measuring s-parameters of a FSS with their advantages and disadvantages have been discussed. The waveguide simulator method was chosen due to building only one cell, therefore, less fabrication work and easier diagnosis. The effect of having four PEC boundaries in a waveguide simulator compared to ideal case where there are both PEC and PMC boundaries have been discussed.

Most of the time was spent for the fabrication part of the project. Following issues were faced in the process of fabricating the FSS unit cell:

1. Lithography development for small features (5 µm) beside large features (20 µm).
2. Selection of the sacrificial layer material.

3. Development of techniques to release a suspended MEMS structure.

4. Insulation layer to spate the bias line from the waveguide simulator.

And many other problems were solved in the thesis.

The measurement results showed two major problems with the initial fabricated device. First, the contaminated sacrificial layer weakened the reflected wave. Second, neglecting the bias line in the first simulation run caused a noticeable difference in the measured and simulated resonance frequencies. Further study was done to explain the difference in the initial design and measurement results.

Finally, a new FSS design is proposed, which resolves the issues of the first design. The new design is based on:

1. Re-designing the FSS dimensions to operate in X-band frequency range with inclusion of the effect of the bias line.

2. Development of an alternate MEMS bridge structure with spring arms to achieve a better flexibility, lower the actuation voltage, and improve EM bandwidth.

Future works are:

1. Using PECVD to deposit a good quality silicon sacrificial layer, and thermal oxidation to deposit a good quality silicon dioxide layer.

2. Fabricating an array of the designed FSS unit cell and designing a bias line network to actuate each element.

References

[1] B. Schoenlinner, A. Abbaspour-Tamijani, L. C. Kempel, and G. M. Rebeiz, "Switchable Low-Loss RF MEMS Ka-Band Frequency-Selective Surface," *IEEE Transactions on Microwave Theory and Techniques*, vol. 52, no. 11, pp. 2474-2481, Nov. 2004.

[2] J. M. Zendejas, J. P. Gianvittorio, Y. Rahmat-Samii, and J. W. Judy, "Magnetic MEMS Reconfigurable Frequency-Selective Surfaces," *Journal of Microelectromechanical Systems*, vol. 15, no. 3, pp. 613-623, Jun. 2006.

[3] M. J. Madou, *Fundamentals of microfabrication: the science of miniaturization*. CRC Press, 2002, p. 723.

[4] J. D. Plummer, M. D. Deal, and P. B. Griffin, *Silicon VLSI technology: fundamentals, practice and modeling*. Prentice Hall, 2000, p. 817.

[5] B. Bahreyni, "Design, modeling, simulation, and testing of resonant micromachined magnetic field sensors," University of Manitoba, 2006.

[6] J. Yip, "MEMS micro-ribbons for integrated ground plane microstrip delay line phase shifter," University of Manitoba, 2008.

[7] G. M. Rebeiz and J. B. Muldavin, "RF MEMS switches and switch circuits," *IEEE Microwave Magazine*, vol. 2, no. 4, pp. 59-71, 2001.

[8] C. Goldsmith et al., "Characteristics of micromachined switches at microwave frequencies," in *1996 IEEE MTT-S International Microwave Symposium Digest*, vol. 2, pp. 1141-1144.

[9] G. M. Rebeiz, *RF MEMS: theory, design, and technology*. John Wiley and Sons, 2003, p. 483.

[10] L. E. Larson, R. H. Hackett, M. A. Melendes, and R. F. Lohr, "Micromachined microwave actuator (MIMAC) technology-a new tuning approach for microwave integrated circuits," in *IEEE 1991 Microwave and Millimeter-Wave Monolithic Circuits Symposium. Digest of Papers*, pp. 27-30.

[11] C. B. Wheeler, "Latching micromagnetic relays," *Journal of Microelectromechanical Systems*, vol. 10, no. 4, pp. 511-517, 2001.

[12] B. Munk, R. Kouyoumjian, and L. Peters, "Reflection properties of periodic surfaces of loaded dipoles," *IEEE Transactions on Antennas and Propagation*, vol. 19, no. 5, pp. 612-617, Sep. 1971.

[13] B. A. Munk, *Frequency selective surfaces: theory and design*. John Wiley and Sons, 2000, p. 410.

[14] R. Mittra, C. H. Chan, and T. Cwik, "Techniques for analyzing frequency selective surfaces-a review," *Proceedings of the IEEE*, vol. 76, no. 12, pp. 1593-1615, 1988.

[15] L. B. Whitbourn and R. C. Compton, "Equivalent-circuit formulas for metal grid reflectors at a dielectric boundary," *Applied Optics*, vol. 24, no. 2, p. 217, Jan. 1985.

[16] J. Huang, "Microstrip reflectarray," *Antennas and Propagation Society Symposium 1991 Digest*, pp. 612-615, 1991.

[17] T. K. Chang, R. J. Langley, and E. A. Parker, "Frequency selective surfaces on biased ferrite substrates," *Electronics Letters*, vol. 30, no. 15, p. 1193, 1994.

[18] A. C. de C. Lima, E. A. Parker, and R. J. Langley, "Tunable frequency selective surface using liquid substrates," *Electronics Letters*, vol. 30, no. 4, p. 281, 1994.

[19] D. S. Lockyer and J. C. Vardaxoglou, "Reconfigurable FSS response from two layers of slotted dipole arrays," *Electronics Letters*, vol. 32, no. 6, p. 512, 1996.

[20] T. K. Chang, R. J. Langley, and E. Parker, "An active square loop frequency selective surface," *IEEE Microwave and Guided Wave Letters*, vol. 3, no. 10, pp. 387-388, 1993.

[21] K. D. Stephan, F. H. Spooner, and P. F. Goldsmith, "Quasioptical millimeter-wave hybrid and monolithic PIN diode switches," *IEEE Transactions on Microwave Theory and Techniques*, vol. 41, no. 10, pp. 1791-1798, 1993.

[22] J. C. Vardaxoglou, "Optical switching of frquency selective surface bandpass response," *Electronics Letters*, vol. 32, no. 25, p. 2345, 1996.

[23] C. Mias, "Varactor tunable frequency selective absorber," *Electronics Letters*, vol. 39, no. 14, p. 1060, 2003.

[24] B. Bahreyni, "Deep etching of silicon with XeF2," University of Manitoba, 2001.

[25] P. B. Chu et al., "Controlled pulse-etching with xenon difluoride," in *Proceedings of International Solid State Sensors and Actuators Conference (Transducers '97)*, vol. 1, pp. 665-668.